FABRICATION AND CHARACTERIZATION OF $BiVO_4$-BASED PHOTOANODES FOR USE IN PHOTOELECTROSYNTHETIC SOLAR CELLS

by

Jacob N. Wortley

Submitted in partial fulfillment of the

requirements for Departmental Honors in

the Department of Chemistry & Biochemistry

Texas Christian University

Fort Worth, Texas

May 8, 2023

FABRICATION AND CHARACTERIZATION OF $BiVO_4$-BASED PHOTOANODES FOR USE IN PHOTOELECTROSYNTHETIC SOLAR CELLS

Project Approved:

Supervising Professor: Benjamin Sherman, Ph.D.

Department of Chemistry & Biochemistry

Chair of Department: Benjamin Janesko, Ph.D.

Department of Chemistry & Biochemistry

David Minter, Ph.D.

Department of Chemistry & Biochemistry

Shauna McGillivray, Ph.D.

Department of Biology

ABSTRACT

A photoelectrosynthetic solar cell is a device that converts light energy into chemical potential energy by driving an overall endothermic reaction, such as benzyl alcohol dehydrogenation. To catalyze these reactions, visible light-absorbing metal oxide semiconductor materials such as $BiVO_4$, α-Fe_2O_3, and WO_3 are often utilized. This work describes the fabrication and study of nanostructured $BiVO_4$-based photoanodes to optimize the capture and conversion of light energy to chemical potential energy. Two approaches are explored for improving the photoelectrochemical (PEC) performance of $BiVO_4$-based photoanodes: 1) increasing the surface area of the $BiVO_4$ interface through the use of a structure directing agent (polyethylene glycol) and 2) the use of a heterojunction WO_3|$BiVO_4$ interface.

To investigate the hypothesis that increased $BiVO_4$ surface area would improve the photocurrent generated, the concentration of polyethylene glycol (PEG), used as a templating agent, was changed in the $BiVO_4$ deposition solution. Specifically, this study describes the fabrication of FTO|$BiVO_4$ surfaces from solutions containing varying PEG concentrations by weight (2.5% w/w and 5% w/w) to determine the relationship between porosity and the resultant photocurrent generation. These nanostructured photoanodes were used to measure the oxidation of (2,2,6,6-tetramethylpiperidin-1-yl)oxyl (TEMPO), via PEC analysis. While the concentration of polymer did increase the porosity and surface area of the $BiVO_4$ films, decreased photocurrents were observed for high surface area films compared to those with smaller surface areas.

The second approach to improving PEC performance involves establishing a type II heterojunction interface using sequential deposition of WO_3 and $BiVO_4$ layers on the electrode surface. Based on the conduction band alignment of these materials, photoexcited electrons from $BiVO_4$ should transfer to WO_3 while holes accumulate at the $BiVO_4$-electrolyte interface.

Information about the efficiency of light energy conversion to chemical energy was obtained by incident photon-to-current (IPCE) measurements. IPCE values are determined by relating the proportion of incident light power to the current produced by illuminating the WO_3-$BiVO_4$ photoanode over a small wavelength range. IPCE experiments were run for WO_3-only, $BiVO_4$-only, and WO_3-$BiVO_4$ samples. It was hypothesized that the WO_3-$BiVO_4$ heterojunction will increase the conversion of light energy into chemical energy. Comparing IPCE values for WO_3-$BiVO_4$ samples shows a clear increase compared to $BiVO_4$-only photoanodes. These results demonstrate how coupled materials (WO_3-$BiVO_4$) can generate higher current densities upon illumination for driving photoelectrosynthetic reactions. Overall, these two approaches provide valuable insight into the optimization of $BiVO_4$-based photoanodes for use in photoelectrosynthetic solar cells.

ACKNOWLEDGEMENTS

I want to give my dearest thanks to Dr. Ben Sherman and Dr. Nelli McMillan for their continuous support and expertise throughout my time as a research assistant. With their guidance, I have developed into the scientist and student I have always dreamed of becoming. By inspiring curiosity, I am better equipped to accomplish the goals I have set for my future career as a life-long learner. Additionally, I would like to thank the Department of Chemistry and the Department of Biology for providing me with a world-class education and guiding my academic journey. Lastly, I thank my loving family and late father, who, through their love, fostered the values I cherish today. Without you, I would not be the man, son, brother, scientist, or future healthcare professional I strive to be. *Ancora Imparo*

TABLE OF CONTENTS

LIST OF FIGURES

LIST OF EQUATIONS AND TABLES

Chapter I: Effect of Polyethylene Glycol on the Fabrication of Nanostructured $BiVO_4$ Photoanodes for Photoelectrochemical-Mediated Oxidations

Introduction

Light-driven reactions, such as those utilized in photoelectrosynthetic applications, focus on capturing and transferring light energy to drive chemical reactions. For this purpose, light-active metal oxide semiconductor materials are used, such as bismuth vanadate ($BiVO_4$), tungsten oxide (WO_3), and hematite (α-Fe_2O_3) to list a few. $BiVO_4$ is a promising semiconductor for solar energy conversion reactions due to its non-toxic properties, low cost, and ability to absorb visible light.[1] To better understand the usefulness of semiconductors, it is essential to recognize how energy moves through various materials. As network covalent solids, semiconductors contain highly degenerate bonding and antibonding molecular orbital levels that organize into filled valence band (VB) and vacant conduction band (CB) orbital levels.[2,3] **Figure 1** presents the difference in relative band alignments of insulating, semiconducting, and conducting materials. The valence and conduction bands overlap in metals, as seen in **Figure 1a**. This creates a continuous distribution of electronic states, with no energy gaps, making metals conductive at all energies.

Conversely, insulators (**Fig. 1c**) have a more significant energy difference between the VB and CB. Because of this large band gap, significant energy is required to excite electrons from the VB to the CB.[2,3] The lack of available orbitals in the band gap energy range makes these materials nonconductive, unlike metals such as copper or iron. However, semiconductors such as $BiVO_4$ and WO_3 (**Fig. 1b**) differ in that the band gap (measured in electron volts) is in between that of conductors and insulators.[2] In other words, semiconductors will behave as conductors, but only at energies within the valence band or conduction band levels.

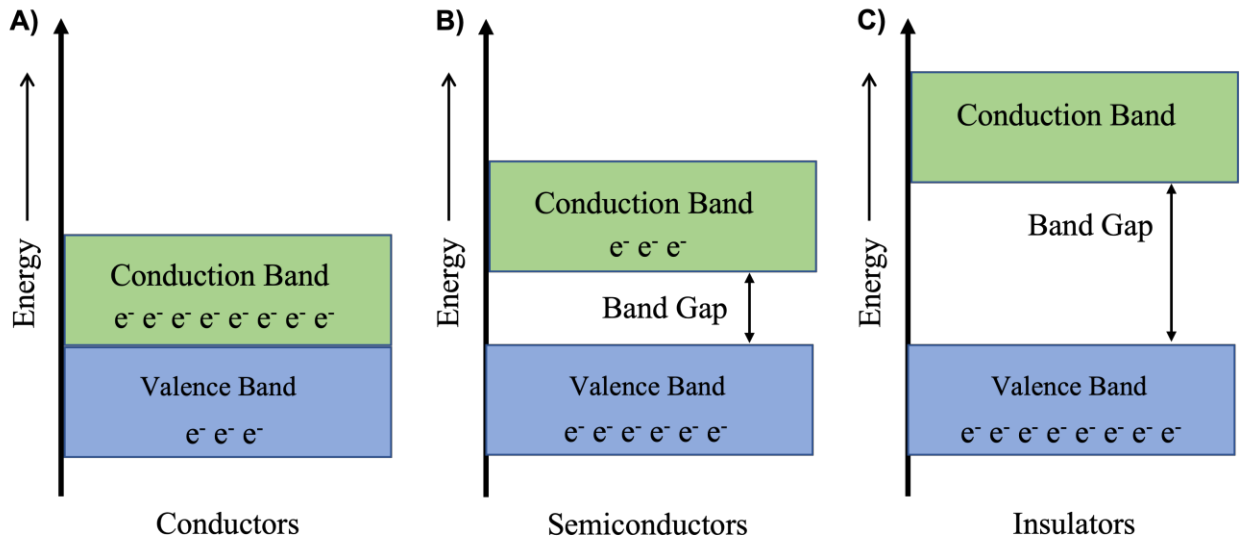

Figure 1. Energy band diagrams indicating the position of valence and conduction bands with associated band gaps for the following material types: A) conductors, B) semiconductors, and C) insulators.

This work utilizes semiconductors with a band gap capable of absorbing visible light. Specifically, the monoclinic scheelite crystal form of $BiVO_4$ prepared in this work exhibits a band gap of 2.4 eV, corresponding to excitation by light of a wavelength less than 520 nanometers.[4-6] Given that the visible light spectrum spans from 400-700 nm wavelength, the $BiVO_4$ semiconductors described in this study capture approximately 11% of the visible spectrum.[3] This is particularly advantageous for photoelectrosynthesis as more of the visible light spectrum can be utilized to facilitate the formation of the desired products.[7]

In addition to the advantages listed above, monoclinic $BiVO_4$ semiconductors exhibit properties of an n-type semiconductor. Generally, two types of semiconductors are of industrial importance: n-type and p-type. These semiconductors exhibit different Fermi levels, or the energy where the probability of finding a filled orbital is 50%.[2] In the context of light-active semiconductors, the position of the Fermi level relative to the conduction and valence band edges

determines the efficiency of the solar cell, as it affects the direction of electron flow under illumination. For intrinsic semiconductors that do not exhibit n- or p-type properties, the fermi level exists at an energy level halfway between the filled VB and vacant CB. In p-type semiconductors, the Fermi level is positioned closer to the valence band, as shown in **Fig. 2a**. This creates an excess of holes, or the absence of an electron, within the VB.[2] Upon light excitation of a p-type system, high electron mobility results in good conductivities in the valence band.[8]

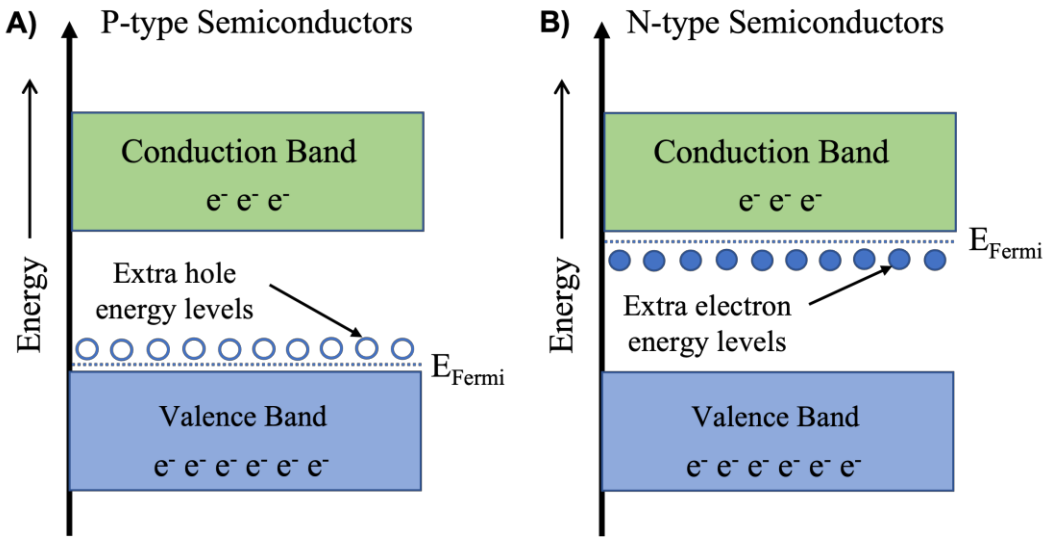

Figure 2. Energy band diagram showing the position of valence bands, conduction bands, and the associated fermi level positions for A) p-type semiconductors and B) n-type semiconductors (similar to $BiVO_4$). Additionally, this figure shows the presence of extra electron energy levels in n-type semiconductors as well as extra hole energy levels in p-type semiconductors.

Conversely, n-type semiconductors such as WO_3 and $BiVO_4$ exhibit a fermi level closer to the CB, resulting in high electron mobility and conductivity in the conduction band. Thus, photo-excited electrons are free to move through the conduction band under an applied bias to catalyze a chemical reaction. While n- and p-type semiconductors typically require the presence of a dopant atom that either donates or accepts electrons, monoclinic $BiVO_4$ exhibits morphological defects that create donor orbitals near the CB edge.[7,9,10] Defect sites, such as an oxygen atom vacancy or

a grain boundary where two monoscheelite domains meet but are misaligned, create local orbitals that can act similarly to a dopant atom used in developing n- and p-type semiconductors.[2]

As illustrated in **Fig. 2b**, the higher energy fermi level assists the flow of electrons into the conduction band to increase photocurrent generation when excited by light of a sufficient wavelength (i.e., less than 520 nm in the case of $BiVO_4$). Under these conditions, an electron-hole pair is produced that can migrate to the interface and participate in subsequent redox reactions.[2] In this work, electrons excited in the $BiVO_4$ photoanode layer are collected at the FTO ohmic contact while photogenerated holes migrate to the $BiVO_4$ surface and drive the oxidation of an N-oxyl catalyst, TEMPO.[1] TEMPO, as discussed later, serves as a redox mediator that facilitates subsequent reactions discussed later in this work.

While $BiVO_4$ has many advantages as a candidate for running controlled, photo-induced oxidations, its main disadvantage lies in its tendency to undergo electron recombination.[1] During recombination, electron and hole pairs created after photon absorption recombine via bulk or surface-mediated recombination pathways before the charges can drive current flow in the cell.[11,12] In bulk recombination, an electron excited to the CB returns to a vacant orbital in the VB producing heat.[2] More commonly, $BiVO_4$ undergoes surface recombination.[1] This occurs when photo-excited electrons in the CB recombine with vacant orbitals localized at the semiconductor–electrolyte interface.[3] A thinner and lower surface area morphology may reduce this recombination, thereby increasing the charge separation efficiency to allow charge transfer with the redox mediator.[1] This work focuses on using polyethylene glycol (PEG) as a structure-directing agent to control the thickness and average particle size of $BiVO_4$ films formed using a liquid-phase deposition method.

This study examines the oxidative performance of $BiVO_4$ photoanodes formed from deposition solutions containing varying concentrations of the structure-directing polymer,

polyethylene glycol (PEG). PEG is a helpful agent in altering film thickness, porosity, and surface area. It can direct structural features as it is mixed within the $BiVO_4$ precursor solution, deposited on an electrode surface, and later burned off in a sintering process. By sintering the samples at a specific time and temperature, the monoclinic scheelite crystal forms around the interdigitated PEG. Since the co-deposited PEG subsequently burns off during the high-temperature thermal curing, a highly porous and large surface area $BiVO_4$ coating is formed.[5] By testing different concentrations of PEG polymer added to the precursor solution with different chain length PEG samples, various $BiVO_4$ surface morphologies can be generated, and the oxidative performance measured and compared across the sample types. The two sample types tested here use a solution containing either 2.5% or 5% by weight (w/w) PEG in the $BiVO_4$ precursor solution. It was hypothesized that FTO|$BiVO_4$(2.5%) electrodes would exhibit lower surface area coatings, improving oxidative performance.

Once $BiVO_4$ semiconductor electrodes were fabricated, their photoelectrochemical (PEC) performance was measured using standard electrochemical methods with 2,2,6,6-tetramethylpiperidin-1-yl)oxyl (TEMPO) added to the electrolyte solution. TEMPO functions as a sacrificial donor, enabling the photogenerated holes localized at the $BiVO_4$ surface to extract electrons from the electrolyte and form $TEMPO^+$. Once oxidized via heterogeneous electron transfer with the $BiVO_4$ surface (**Fig. 3**), $TEMPO^+$ can catalyze the oxidation of organic species in solution, such as the conversion of benzyl alcohol to benzaldehyde. Recent literature in photoelectrochemical reactions has focused on the oxidative production of value-added chemicals (i.e., benzaldehyde) coupled with hydrogen production.[1] A redox mediator such as TEMPO can produce valuable compounds like benzaldehyde at lower overpotentials while simultaneously forming cathodic hydrogen gas.[13-15] As a competent catalyst for the oxidation of an alcohol to an

aldehyde, this redox mediator also prevents the formation of competing oxidative byproducts formed at the $BiVO_4$ surface by selectively reacting with surface holes.[14,15] Unlike many common oxidizing agents, $TEMPO^+$ avoids the production of benzoic acid, a carboxylic acid derivative following two, two-electron oxidations of the starting alcohol, thus improving the yield of benzaldehyde. **Figure 3** illustrates the role of TEMPO as a redox mediator to catalyze the formation of benzaldehyde upon the photoexcitation of electrons within the $BiVO_4$ semiconductor.

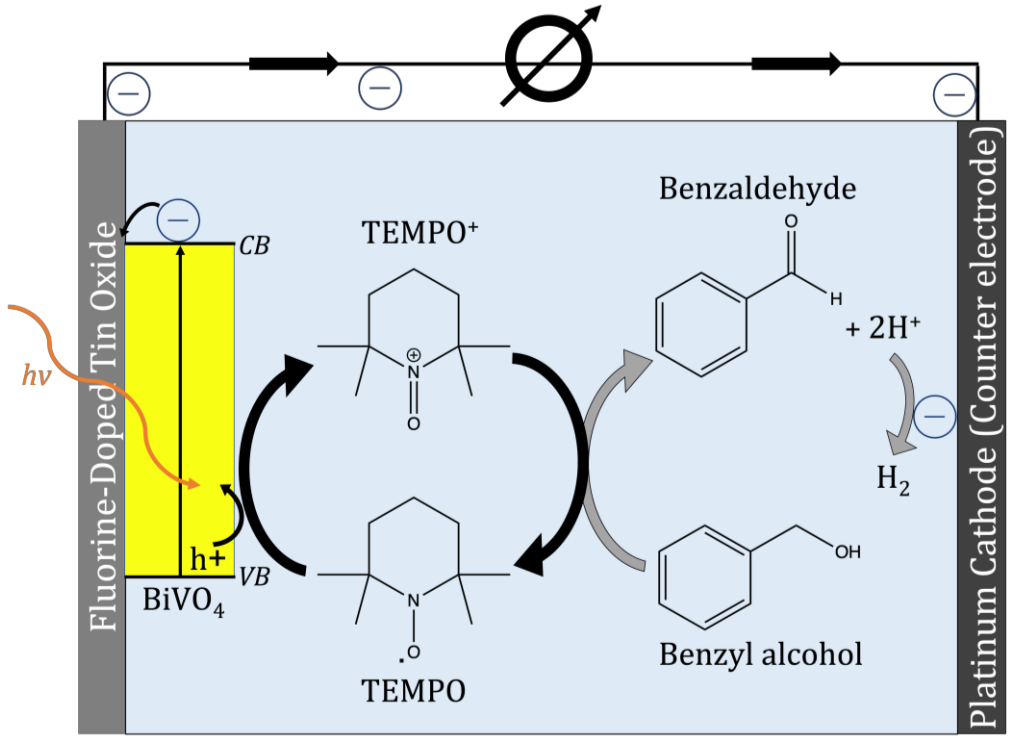

Figure 1. Schematic of PEG-structured $BiVO_4$ photoanodes in solution illustrating the light-driven oxidation of TEMPO to $TEMPO^+$ in addition to the subsequent oxidation of benzyl alcohol to benzaldehyde. This diagram includes the FTO ohmic contact as well as the platinum cathode with labeled electron movement and cathodic hydrogen production.

To better understand the effect of varying concentrations of PEG on the $BiVO_4$ films, experimental data on linear sweep voltammetry, cyclic voltammetry, chronoamperometry, and open circuit potential were analyzed in a TEMPO solution without benzyl alcohol. These tests provide insight into the nuances of electron transport through $BiVO_4$ and its subsequent oxidation

of TEMPO in solution to aid in understanding how the addition of PEG affects the photoelectrochemical performance of the $BiVO_4$-based photoanode.[13]

Methods

Materials

Bismuth (III) nitrate pentahydrate ($Bi(NO_3)_3 \cdot 5H_2O$, 99.999%), ammonium metavanadate (NH_4VO_3, ≥98.0%), nitric acid (70% pure in water, Acros Organics), polyethylene glycol-20,000 (Beantown Chemical), and polyethylene glycol-100,000 (Beantown Chemical) were used in this study. The $BiVO_4$ precursor solution consisted of 2 mmol $Bi(NO_3)_3$ and 2 mmol NH_4VO_3 (1:1 mole ratio) dissolved in 10 mL of an aqueous nitric acid solution (2 M). To avoid reagent aggregation, NH_4VO_3 was added to the mixture with nitric acid and sonicated for 10 minutes until fully dissolved. Next, the $Bi(NO_3)_3$ was added and sonicated for five minutes. PEG (either 20,000 or 100,000 molecular weight, as indicated) was added to give a 2.5 or 5% weight percent solution (typically 140-300 mg of PEG added per 10 mL) of the total precursor solution. Once weighed, PEG was mixed with the $BiVO_4$ precursor solution and sonicated for five minutes to dissolve the polymer. The resultant $BiVO_4$-PEG precursor solution is light-yellow.

Following the preparation of the precursor solution, a liquid-phase deposition (LPD) technique was utilized.[1,16] Fluorine-doped tin oxide (FTO) glass (15 Ω cm^{-2}) (Hartford Glass Co.) was cut into 1 × 4 cm sections and cleaned ultrasonically with ethanol for 15 minutes. A second sonication was completed in 1:1 ethanol/acetone for 15 minutes. The FTO substrates were then dried with pure nitrogen gas before the $BiVO_4$-PEG precursor solution was deposited. Next, the FTO substrate was dipped in the $BiVO_4$-PEG precursor solution for five seconds. The non-conductive side of the FTO was wiped clean of precursor solution after deposition. The samples were left to dry at room temperature until an orange film appeared on the FTO electrode. Sintering

at 450 °C for two hours produced a bright yellow $BiVO_4$ film. The sintered $BiVO_4$ films were treated in a 1 M NaOH bath for 30 minutes, followed by a rinse with ultrapure water (18 MΩ), and drying with nitrogen gas.[7] An epoxy border was applied to produce circular areas of $BiVO_4$ on the FTO surface for photoelectrochemical analysis. These photo-active areas were later measured to convert the total current output into photocurrent density for comparative analysis across sample types. The CG electrodes were fabricated by epoxying an FTO working electrode to another FTO substrate with a ~ 1 mm gap in between them. This setup allows for a small volume of electrolyte/TEMPO solution to remain in the CG spacer to track the generation of $TEMPO^+$ at the FTO generator electrode and subsequent reduction back to TEMPO at the FTO collector electrode (**Fig. 13**).

Characterization Methods

Ultraviolet-Visible (UV-Vis) absorption spectroscopy was used to measure the absorbance of the fabricated samples using a previously outlined procedure.[1] An Agilent Technologies Cary 60 spectrometer, with measurements baselined to clean FTO, was used for all measurements. Spectra were collected from 900 nm to 200 nm. The resultant absorbance spectra were utilized to extrapolate Tauc plots and estimate the band gap energy of the material.

In addition to collecting light absorbance data of these $BiVO_4$-PEG photoanodes, the surface morphology was assessed via a JEOL JSM61000 Field Emission Scanning Electron Microscope (FESEM, or SEM) under an accelerated voltage of 5 kV.[17] Samples were sputtered with a 10 nm layer of gold prior to FESEM characterization.

Photoelectrochemical Studies

Cyclic voltammetry (CV), linear sweep voltammetry (LSV), open circuit potential (OCP), chronoamperometry (CA), and collector-generator (CG) experiments were conducted to test the

$BiVO_4$ surfaces. A WaveNow® potentiostat (Pine Instruments) was used for all photoelectrochemical measurements using a three-electrode configuration with the $BiVO_4$-based photoanode as a working electrode, an Ag/Ag^+ quasi-reference electrode, and a Pt counter electrode, all held at room temperature. All illumination experiments were completed with AM 1.5G simulated solar light at an intensity of 100 mW cm^{-2} using a Newport Oriel LSH-7320 LED lamp. The Ag/Ag^+ quasi-reference electrode was calibrated vs. ferrocenium/ferrocene that was added to the experimental mixture after PEC measurements. The calibrated potential scale was then converted to the saturated calomel electrode (SCE) scale using $E'(Fc^+/Fc) = 0.45$ V vs. SCE. All illumination was conducted in 10 mL of solution with backside illumination of the working electrode. The electrolyte solution contained acetonitrile with 0.1 M tetrabutylammonium hexafluorophosphate ($TBAPF_6$) and 5 mM TEMPO. The $TBAPF_6$ was doubly recrystallized from absolute ethanol and stored in a desiccator before use in all PEC measurements. All CV and LSV experiments were taken at a scan rate of 50 mV s^{-1} unless otherwise noted. CV was completed across an applied bias starting at 0 V, increasing to 1.4 V, and then decreasing to -0.4 V unless otherwise noted. LSV measurements were taken at a sweep of applied biases from 1 V to -0.4 V. OCP measurements recorded under dark/light conditions all began in the dark for 20 s, received 100 mW cm^{-2} white light illumination for 30 s, then returned to dark for the remainder of the experiment. Photocurrent measurements carried out via chronoamperometry were performed at 0.3 V vs. SCE with 30 s on/off chopped illumination. Collector-generator (CG) experiments were conducted using CV parameters with increasing scan rates of 10, 25, 50, 75, and 100 mV s^{-1}. The geometric surface area of the working electrodes was typically about 0.4 cm^2 and was used to convert the current output to a current density of the sample.

Results/Discussion

Fabrication of PEG-based $BiVO_4$ Photoanodes

Fabrication of PEG-based $BiVO_4$ electrodes followed a simple liquid-phase deposition method and sintering protocol as shown in **Fig. 4**. Sintering is an important step in the production of $BiVO_4$ electrodes. This process involves heating the $BiVO_4$ precursor molecules below their melting point to allow for atoms to diffuse and form large, crystalline units that improve electronic properties.[18] Sintering temperature and time directly affect the resultant surface morphology, and studies have reported that sintering the $BiVO_4$ precursor solution at 450 °C for 45 minutes facilitates the growth of monoclinic scheelite crystals.[1,19] As discussed previously, monoclinic scheelite $BiVO_4$ is advantageous in this work due to its low band gap energy (2.4 eV) and capability to absorb in the visible light spectrum. In addition to altering structural morphology through sintering parameters, this process also burns off interdigitated PEG in the $BiVO_4$ precursor. As discussed previously, the removal of PEG during thermal curing results in high surface area $BiVO_4$ electrodes.

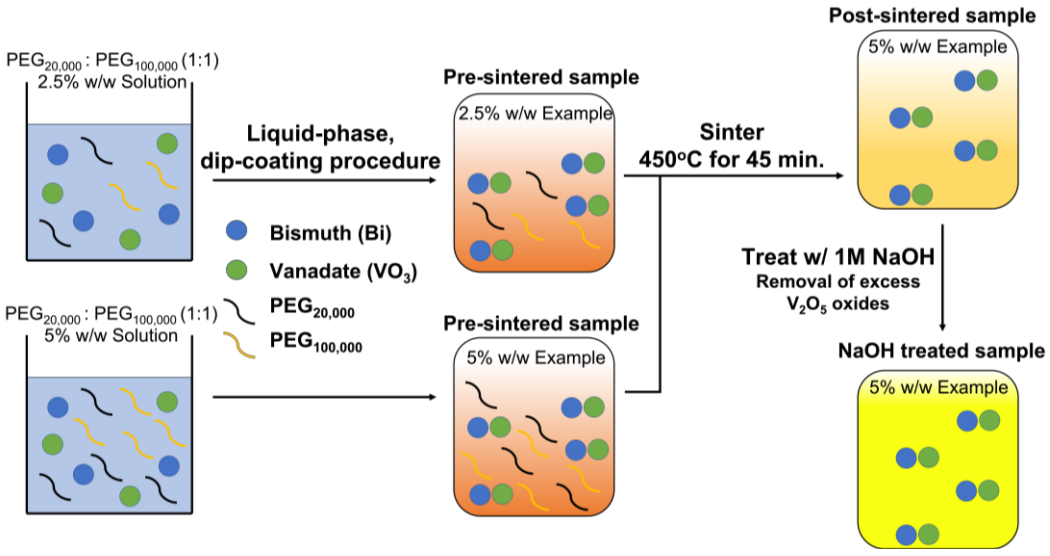

Figure 4. Schematic showing the procedure for fabricating PEG-based $BiVO_4$ electrodes. 2.5% or 5% PEG was added followed by sintering and NaOH treatment to yield a bright yellow $BiVO_4$ electrode.

Once samples underwent thermal curing and removal of PEG, they were then treated with a NaOH bath shown in **Fig. 5a**. This solution treatment removes excess V_2O_5 byproduct from the surface of the sintered $BiVO_4$ electrode. V_2O_5 facilitates the transport of holes and results in an increase in charge carrier recombination within $BiVO_4$ under illumination.[20] Removal of V_2O_5 altered the appearance of the electrodes from yellow-orange to bright yellow. Following NaOH treatment, non-conductive epoxy was applied to the $BiVO_4$ films to produce discrete reaction areas as shown in **Fig. 5b**.

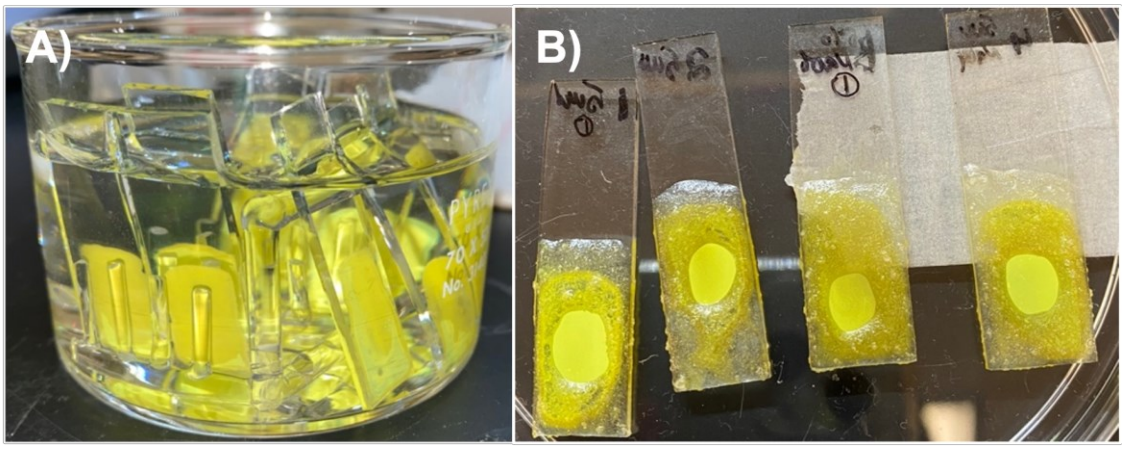

Figure 5. Post-sintered PEG-structured $BiVO_4$ samples. A) Post-sintered samples submersed in a 1M NaOH bath to remove excess V_2O_5. B) Epoxied samples with a circular working area for photoelectrochemical experimentation.

Collector-generator cells were fabricated to determine the collection efficiency of the oxidized-$TEMPO^+$ species as well as calculate its diffusion coefficient. **Figure 6** presents images of this electrode setup. FTO substrates were epoxied face-to-face with a 1 mm glass spacer to produce a small volume gap as shown in **Fig. 6a**. One wire lead was attached to each FTO surface with conductive epoxy in order to measure the generation of $TEMPO^+$ at one FTO electrode and its collection 1 mm away at the other electrode.

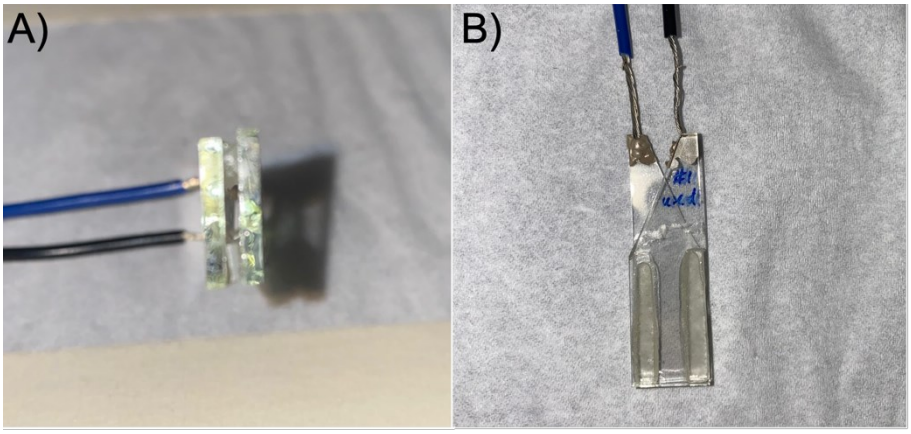

Figure 6. FTO-FTO collector-generator cells with wire leads attached. A) Bottom view of CG cell illustrating the distance gap between the collector and generator electrodes. B) Top view of CG cell showing the stacked FTO design with epoxied spacers.

Physical Characterization of FTO|$BiVO_4$ Photoanodes

UV-Visible spectroscopy was completed to understand the effects of adding variable concentrations of PEG to the precursor solution for forming $BiVO_4$ photoanodes. UV-Vis is a helpful technique to determine the wavelengths of light that a particular material can absorb. The use of UV-Vis in this project focuses on verifying the intrinsic light absorption of monoclinic $BiVO_4$ photoanodes and understanding whether the addition of PEG results in a change in the absorption spectrum. As reported elsewhere,[3,5] the typical light absorption range for $BiVO_4$ photoanodes is around 400-500 nm, corresponding to visible light wavelengths sufficient for electrons to be excited from the low-energy valance band into the higher-energy conduction band. Within a UV-Vis spectrum, the x-axis corresponds to the incident light wavelength graphed against absorption (in absorbance units, A.U.). As illustrated in **Fig. 7a**, the FTO|$BiVO_4$(2.5%) and FTO|$BiVO_4$(5%) exhibited a light absorption onset at approximately 500 nm. Following analysis of UV-Vis data, the band gap energy can be determined by examining a Tauc plot of the absorbance data. Since the band gap energy of a semiconductor quantifies the energy required to

excite an electron into the CB, these values are integral to studying photoelectrochemical performance.[6] A Tauc plot is generated using **Equation 1** where hν is the photon energy, E_g is the band gap energy, a is the absorption coefficient, and B is a proportionality constant.[6] The reported absorption coefficient, a, for monoclinic scheelite $BiVO_4$ is ~1×10^5 cm^{-1}.[21]

(1) $$(a \times h\nu)^{1/\gamma} = B(h\nu - E_g)$$

Values of γ that equal ½ or 2 are indicative of the type of electron transition, either as an indirect or direct band gap.[21] For the $BiVO_4$ photoanodes in this study, direct band gap excitation behavior was assumed and a γ of 2 was used per **Equation 2**.

(2) $$(a \times h\nu)^{1/2} = B(h\nu - E_g)$$

By finding a linear fit for the positively sloped line on the Tauc plot, the band gap can be estimated by the x-intercept of the line of best fit. As shown in **Fig. 7B**, band gaps of 2.35 eV and 2.45 eV were identified for FTO|$BiVO_4$(2.5%) and FTO|$BiVO_4$(5%) samples, respectively.

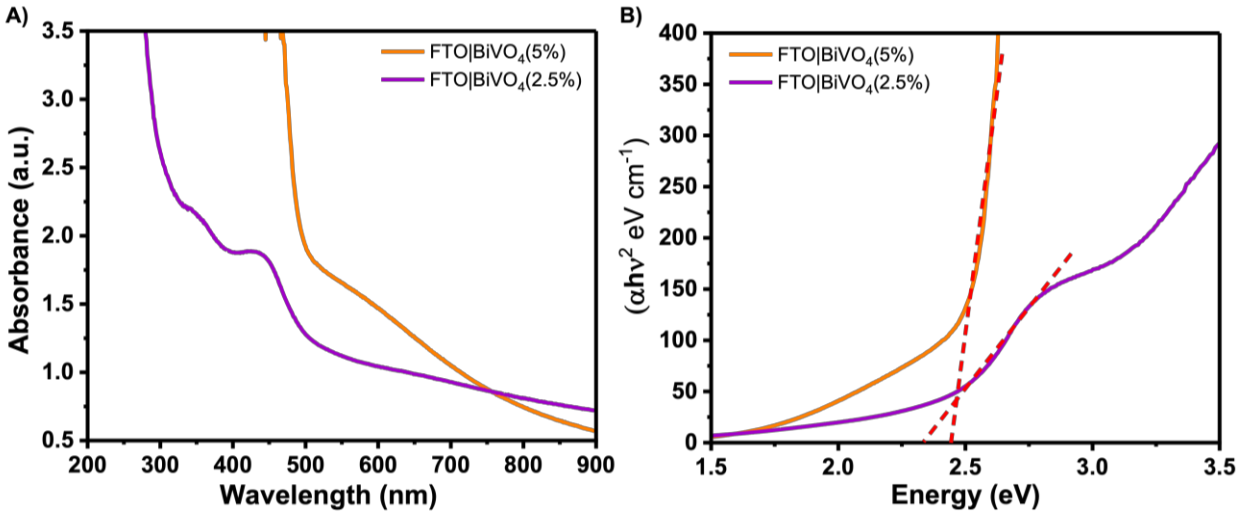

Figure 7. A) UV-Vis absorption spectrum of FTO|$BiVO_4$(2.5%) and FTO|$BiVO_4$(5%) B) Tauc plot extrapolated from UV-Vis measurements with a line of best-fit marking the band gap energy of each sample (E_{gap}).

Following analysis by UV-Vis spectroscopy, the structural morphology of the two sample types was examined using a scanning electron microscope. As shown in **Fig. 8**, the bean-like morphology of monoclinic $BiVO_4$ is consistent across both PEG-directed sample types. Additionally, these structures span from the FTO surface outward, promoting porosity rather than crystallizing in tight sheets with minimal overlap. The bean-like morphology resembles samples made without PEG but exhibits a more porous structure that significantly increases surface area.[5]

While the overall morphological structure of bean-like particles is similar across both PEG concentrations (see **Fig. 8c** and **8d**), a few key differences should be noted. First, the FTO|$BiVO_4$(2.5%) samples exhibited a pitting effect on the outer surface characterized by large circular impressions averaging ~10 μm in diameter. These surface defects are hypothesized to arise from the aggregation of polymer units at the sample surface that was later burned off during the sintering process. It is possible that these polymer units formed micelle-like structures at the outer surface rather than mixing evenly within the $BiVO_4$ precursor, thus resulting in circular deformations. **Figure 8a** shows an SEM image of these surface defects within the FTO|$BiVO_4$(2.5%) photoanodes.

Furthermore, these samples exhibit morphological differences with respect to thickness and bean-width length (a measure of average particle size). As displayed in **Figures 8e** and **8f**, increasing PEG concentrations leads to an overall decrease in film thickness. Specifically, the fabricated FTO|$BiVO_4$(2.5%) samples were approximately ~3.6 μm thick, while the FTO|$BiVO_4$(5%) samples measured ~1.9 μm wide. It should be noted that the thicknesses of the pitted regions were not measured and are likely much thinner than in the measured bulk layer.

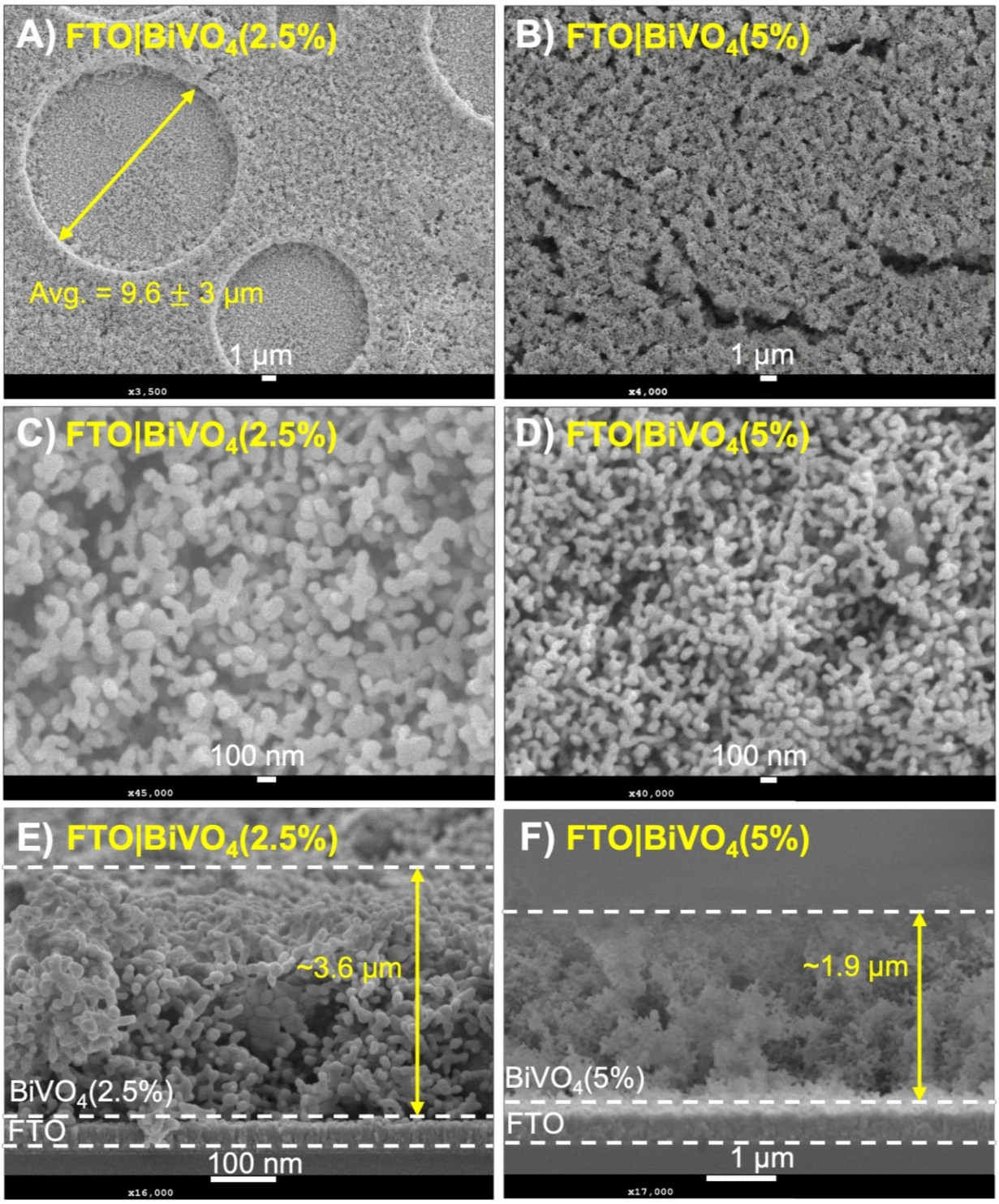

Figure 8. SEM images of PEG-based $BiVO_4$ samples. A) and B) illustrate the top view of FTO|$BiVO_4$(2.5%) and FTO|$BiVO_4$(5%), respectively. C) and D) SEM further magnified top view of FTO|$BiVO_4$(2.5%) and FTO|$BiVO_4$(5%) samples. E) Side view of FTO|$BiVO_4$(2.5%) and FTO|$BiVO_4$(5%) electrode with labeled components and film thickness, respectively.

In addition to the apparent difference in thickness between these two sample types, these photoanodes also differed concerning average bean-like particle width. This measures how wide each crystal particle is within each sample type. Specifically, the FTO|$BiVO_4$(2.5%) photoanodes exhibited an average particle size of 65.8 ± 9 nm, whereas the FTO|$BiVO_4$(5%) samples measured at 50.4 ± 9 nm (see **Fig. 9**). Here, it is essential to note that previous studies without adding PEG exhibited average particle sizes greater than 120 nm.[5,7]

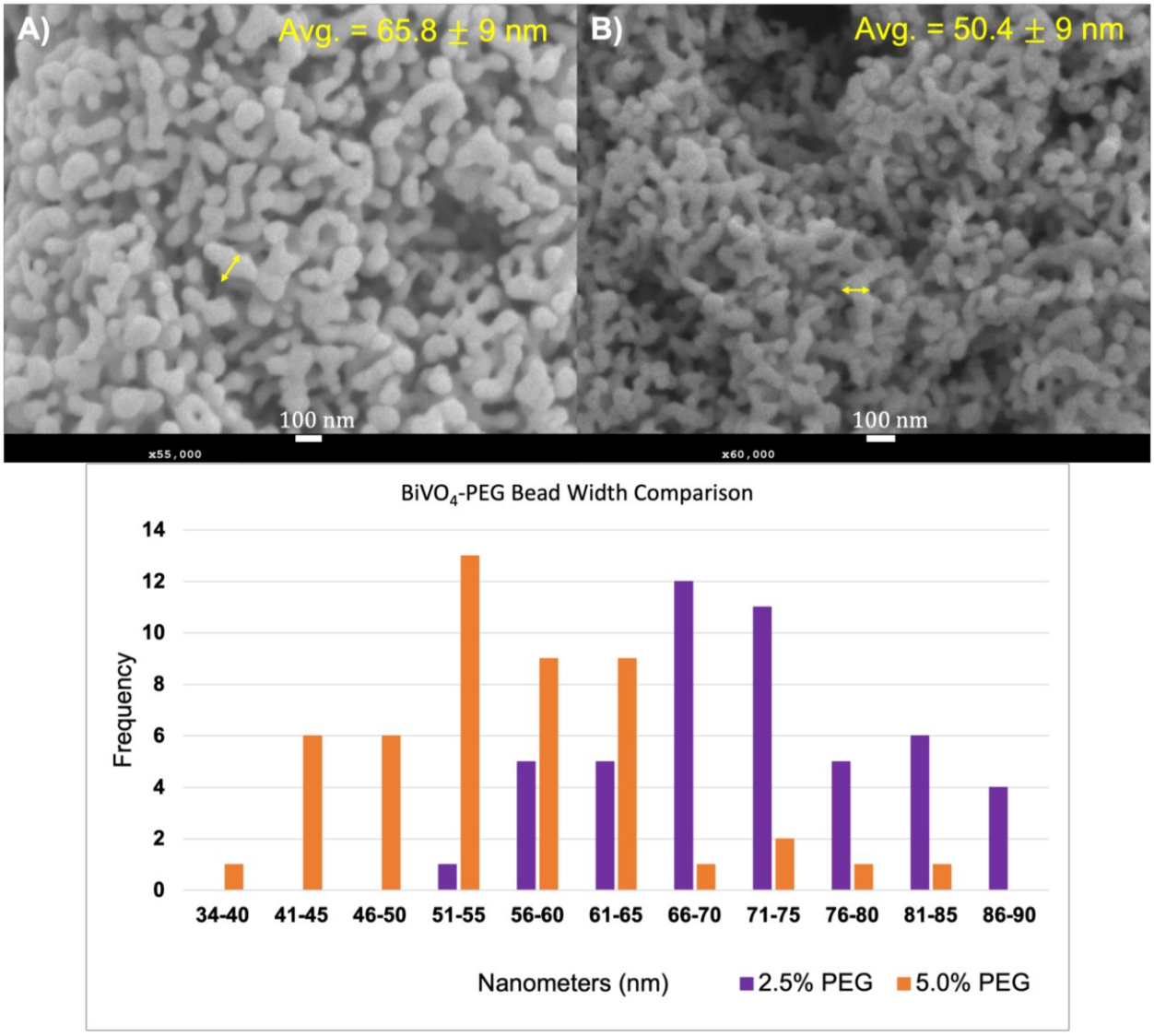

Figure 9. A) and B) illustrate the difference in average particle size of FTO|$BiVO_4$(2.5%) and FTO|$BiVO_4$(5%) samples, respectively. (Bottom) Histogram comparing average particle size between each sample type measured in nanometers (nm).

As evidenced by the SEM images above, the average particle size of the $BiVO_4$ particle domains can be decreased with the addition of the structure-directing agent, PEG. Furthermore, varying the concentration of PEG can change the surface roughness, with the FTO|$BiVO_4$(5%) surfaces showing higher surface areas compared with the FTO|$BiVO_4$(2.5%) samples. **Figure 9c** highlights this idea showing that increasing the concentration of PEG should decrease the average particle size of the resultant $BiVO_4$ photoanode. Overall, SEM surface morphology analysis showed notable differences between FTO|$BiVO_4$(2.5%) and FTO|$BiVO_4$(5%) photoanodes. With the structural differences identified between the two sample types, work then moved on to addressing possible differences in the photoelectrochemical performance as a result of the amount of PEG used to form the FTO|$BiVO_4$ interface.

Photoelectrochemical Performance

After characterization tests, photoelectrochemical performance was experimentally determined for FTO|$BiVO_4$(2.5%) and FTO|$BiVO_4$(5%) sample types. **Figure 10** provides images of the photoelectrochemical cell and labeled electrodes utilized for these studies.

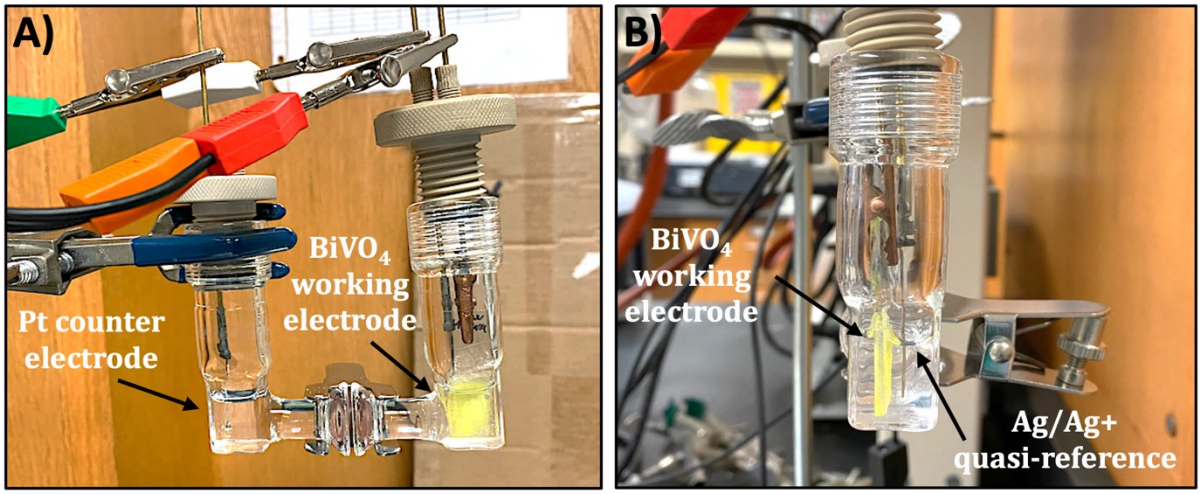

Figure 10. Three-electrode electrochemical setup for running various photoelectrochemical experiments. A) Front view depicting the platinum counter electrode (left) and $BiVO_4$ working electrode (right). B) Side view of working electrode and Ag/Ag^+ quasi-reference electrode.

First, cyclic voltammetry was studied for each sample type in acetonitrile electrolyte and TEMPO. TEMPO was added to the solution as the intended application for these $BiVO_4$ photoanodes is to carry out the light-driven formation of $TEMPO^+$. Generated $TEMPO^+$ can then catalyze controlled organic oxidations such as the conversion of benzyl alcohol to benzaldehyde. Cyclic voltammetry involves sweeping across a range of applied potentials and gathering the resultant current density produced. Having collected measurements of photocurrent density across these potentials, essential findings about charge transfer dynamics and kinetic properties can be assigned. **Figure 11a** shows the cyclic voltammograms (CVs) with 5 mM TEMPO in an organic solution on two different electrode surfaces under dark and illuminated conditions. CV traces for both sample types in the light (solid lines) show a slight anodic signal rising around 0.3 V vs. SCE, indicating the oxidation of TEMPO to $TEMPO^+$ at the $BiVO_4$ surface. This electrochemical process is driven by sunlight and assisted by an applied bias that promotes the transport of photo-excited electrons into the conductive FTO glass. At the same time, electron-deficient holes separate to the surface. These charge-separated holes actively pull electrons from TEMPO in solution, driving the oxidation to $TEMPO^+$.[22]

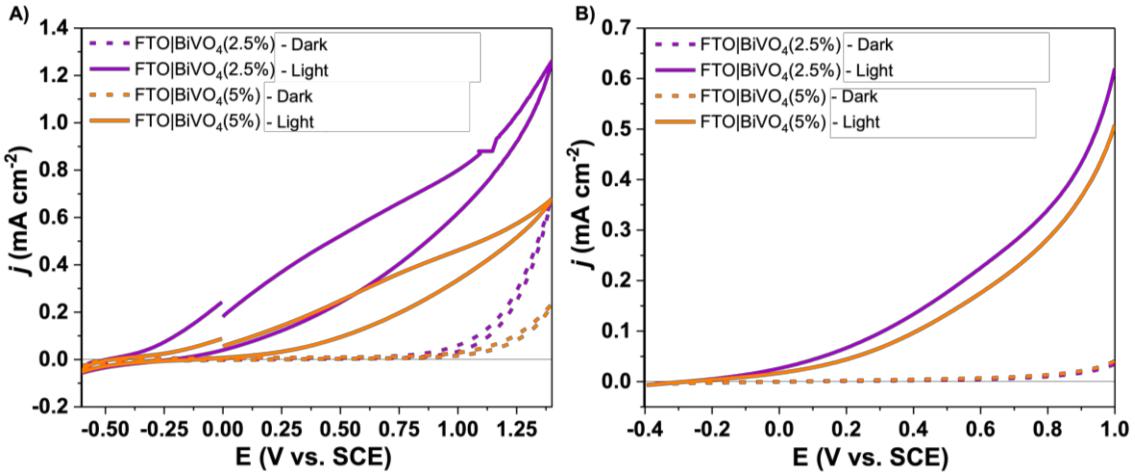

Figure 11. A) Cyclic Voltammetry of FTO|$BiVO_4$(2.5%) and FTO|$BiVO_4$(5%) electrodes in the light and dark in 5 mM TEMPO. A) Linear Sweep Voltammogram of FTO|$BiVO_4$(2.5%) and FTO|$BiVO_4$(5%) photoanodes in the light and dark in 5 mM TEMPO solution.

Since cyclic voltammetry involves sweeping potential in both directions (i.e., from positive to negative and then back), the resultant cathodic peak is also present, indicating the reduction of $TEMPO^+$ back to TEMPO. While these peaks are evident within the voltammogram, this process shows slow kinetic behavior due to the sluggish charge separation within the $BiVO_4$ photoanode.[23,24] This contrasts with materials that support rapid (mass transfer limited) interfacial electron transfer, such as a glassy carbon electrode (**Fig. 15a**) which exhibits sharp anodic and cathodic peaks. Following CV experiments, linear sweep voltammetry (LSV) was utilized to study the prepared samples in dark and illuminated conditions. In contrast to CV, LSV involves sweeping the applied potential from positive to negative potentials to investigate the photoelectrochemical response of these photoanodes. The results from **Fig. 11b** indicate that the FTO|$BiVO_4$(2.5%) (purple solid line) exhibited higher photocurrent density across all applied potential values when illuminated.

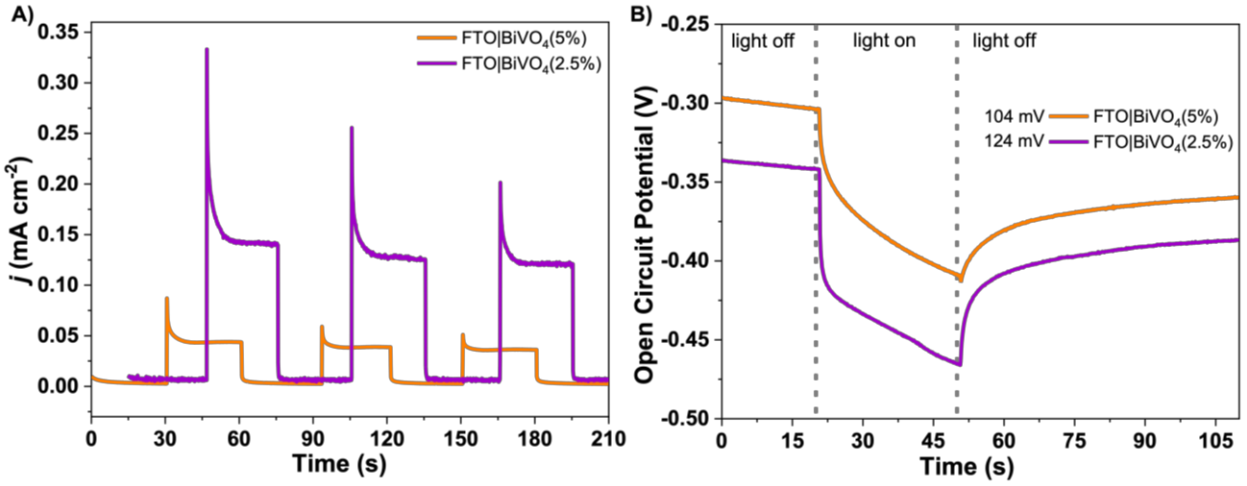

Figure 12. Photoelectrochemical tests were measured in acetonitrile solution containing 5 mM TEMPO in 0.1 M $TBAPF_6$. A) Chronoamperometry (CA) taken under dark and light conditions under an applied bias of 0.3 V vs SCE. Transient photocurrent measurement (j) of FTO|$BiVO_4$(2.5%) is offset on the x-axis for clarity. B) Open circuit potential (OCP) of FTO|$BiVO_4$(2.5%) and -(5%) under dark-light-dark conditions with labeled ΔV_{oc} values in mV.

Following photocurrent analysis across a range of applied potentials, transient photocurrent measurements were taken via chronoamperometric experimentation. For these tests, samples were run in the presence of the redox mediator, TEMPO. Chronoamperometry (CA) measures the current density (**Fig. 12a**) at a fixed applied potential (0.3 V vs. SCE) as a function of dark/light conditions. Quasi-steady state current is achieved approximately 30 seconds after an initial polarization peak. This polarization decrease can be attributed to charge-carrier recombination in bulk or surface trap states of the $BiVO_4$ that compete with hole transfer to the electrolyte.[23] The observed photocurrent is measured after reaching a quasi-steady state to measure the rate at which charge transfer occurs from the sample interface to the solution containing TEMPO. **Table 1** shows the resultant transient photocurrents with the FTO|$BiVO_4$(2.5%) photoanodes outperforming the FTO|$BiVO_4$(5%) samples. This higher photocurrent density can be understood as the result of more efficient charge separation within the photoanode, allowing for the movement of electrons to the FTO interface. At the same time, holes recombine at the surface with electrons from TEMPO. While FTO|$BiVO_4$(2.5%) exhibited the highest photocurrent, it is notably lower than the reported value of 0.28 ± 0.02 mA cm^{-2} for neat-$BiVO_4$ electrodes fabricated using the same protocol.[1]

Table 1. Transient Photocurrent and Open Circuit Potential for FTO|$BiVO_4$(2.5%) and FTO|$BiVO_4$(5%) Electrodes[a]

Electrode Type	j (mA cm^{-2})[b]	ΔV_{oc} (mV)[b]
FTO|$BiVO_4$(2.5%)	$0.095 \pm .04$	158 ± 36
FTO|$BiVO_4$(5%)	$0.039 \pm .01$	108 ± 4

[a] All measurements done in acetonitrile solution containing 5 mM TEMPO in 0.1 M $TBAPF_6$.

[b] Average values for photocurrent and open circuit potential are reported with standard deviation.

Additionally, open circuit potential (OCP) experiments (**Fig. 12b**) were conducted to understand the voltage behavior of the $BiVO_4$ layer in the presence and absence of TEMPO. The chemical equilibrium potential can be determined by studying the potential difference between electrodes while there is no current flowing through the system. The greater the change in OCP upon illumination, the more effective a given $BiVO_4$ surface will be at converting light energy to a charge-separated state. The OCP under illumination represents a dynamic equilibrium of photon absorption exciting electrons from the VB to CB (and making the OCP more negative in potential) balanced against charge recombination (which caused the OCP to shift to more positive potential). **Table 1** indicates that the FTO|$BiVO_4$(2.5%) photoanode resulted in a higher open circuit potential (ΔV_{oc} (mV)). This means that the FTO|$BiVO_4$(2.5%) sample exhibits a higher thermodynamic driving force for the oxidation of TEMPO to $TEMPO^+$. OCP of a photoanode in this work measures the potential difference between the semiconductor $BiVO_4$ surface and the reference electrode in the setup. Thus, a higher OCP means that the surface generates more potential under illumination to drive TEMPO oxidation and corroborates the higher photocurrents observed for these samples.

Collector-generator tests were conducted to try and establish the stability and faradaic efficiency for generating $TEMPO^+$ in solution (**Fig. 13**). The diffusion coefficient, a measure of the mobility of $TEMPO^+$ in the solution, is an important metric for understanding the collector-generator data.[25] By first generating $TEMPO^+$ at the FTO generator-electrode, this oxidized oxoammonium product diffuses across a ~1 mm gap to the collector electrode (FTO) for reduction back to TEMPO. Cyclic voltammograms of the FTO-FTO CG cells (**Fig. 14a**) exhibit sluggish TEMPO oxidation with the lack of an obvious anodic peak at an applied potential of 0.3 V vs. SCE. At larger over-potentials (>0.6 V vs. SCE), the FTO-only electrode oxidizes TEMPO

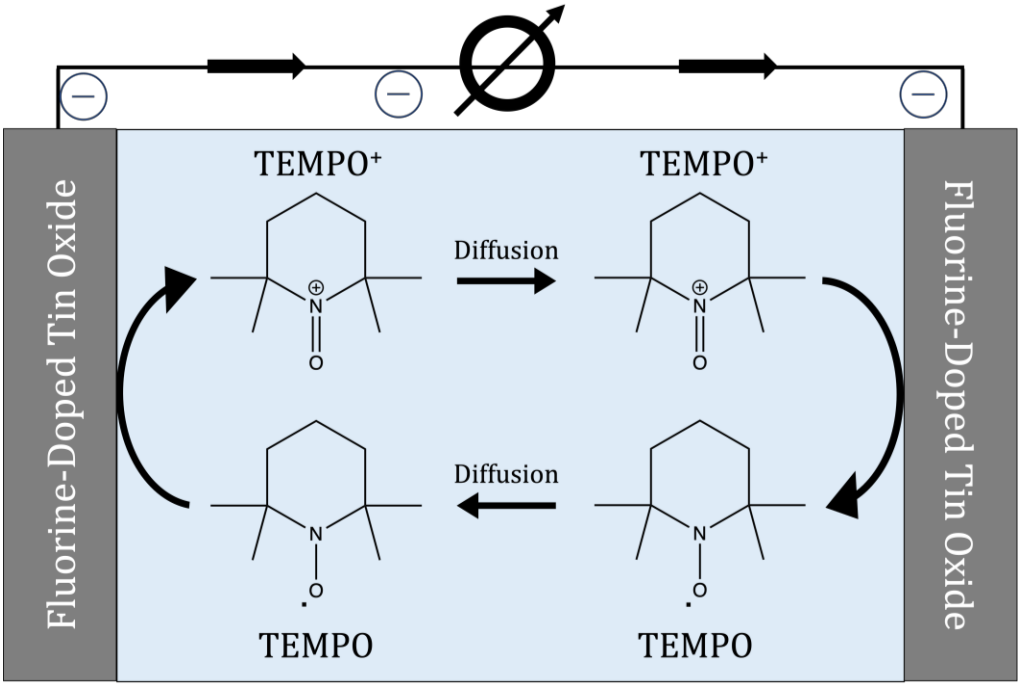

Figure 13. Schematic of collector-generator cell catalyzing the light-driven oxidation of TEMPO to $TEMPO^+$ at the collector-FTO and subsequent back-reduction to TEMPO at the collector-FTO.

more readily than the FTO-FTO CG cell, mostly due to a larger working area of the FTO-only electrode. By integrating the observed photocurrent density over a range of applied potentials, collection efficiency can be plotted, as shown in **Fig. 14b**. Analysis of these results exhibited a 14.6% collection efficiency across the fabricated C-G cell.

Considering the low collection percentage obtained from this setup, further experimentation was conducted to isolate a specific diffusion coefficient of TEMPO. This was completed using a highly sensitive, glassy carbon electrode to measure repeated cyclic voltammograms against varying scan rates of applied potential, as shown in **Fig. 15a**. It is important to note that increased current at increasingly fast scan rates is due to the passing of the same amount of current over smaller time intervals.

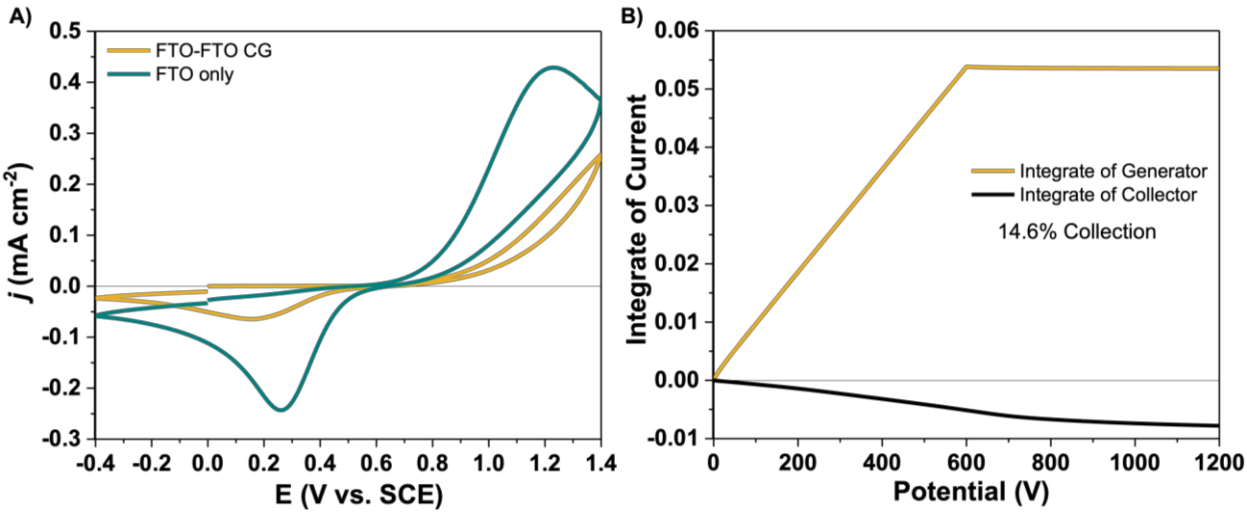

Figure 14. A) Cyclic voltammogram of FTO-FTO collector-generator (orange) and FTO only (blue) in the presence of 5 mM TEMPO. B) Integration of current vs. applied potential graph for the FTO-FTO CG cell used to extrapolate collection % of TEMPO.

Collecting peak anodic photocurrents at various scan rates can then be used to plot observed photocurrent vs. inverse scan rate (**Fig. 15b**). The resultant slope of this linear relationship is then used to calculate the diffusion coefficient of TEMPO in solution via **Equation 3** where j_p is peak anodic current, 2.69×10^5 is a constant (C mol^{-1} V$^{1/2}$), n is the number of moles, A is the electrode area, D_0 is the TEMPO diffusion coefficient, C_0 is the bulk solution concentration, and v is the experimental scan rate.

$$j_p = (2.69 \times 10^5) n^{3/2} A D_o^{1/2} C_0 (v^{1/2}) \quad (3)$$

Extrapolation of this value from **Figures 15a** and **15b** yielded a diffusion coefficient of 1.4×10^{-5} cm^2 s^{-1}. This corresponds to the rate at which TEMPO$^+$ diffuses across a particular distance over time.

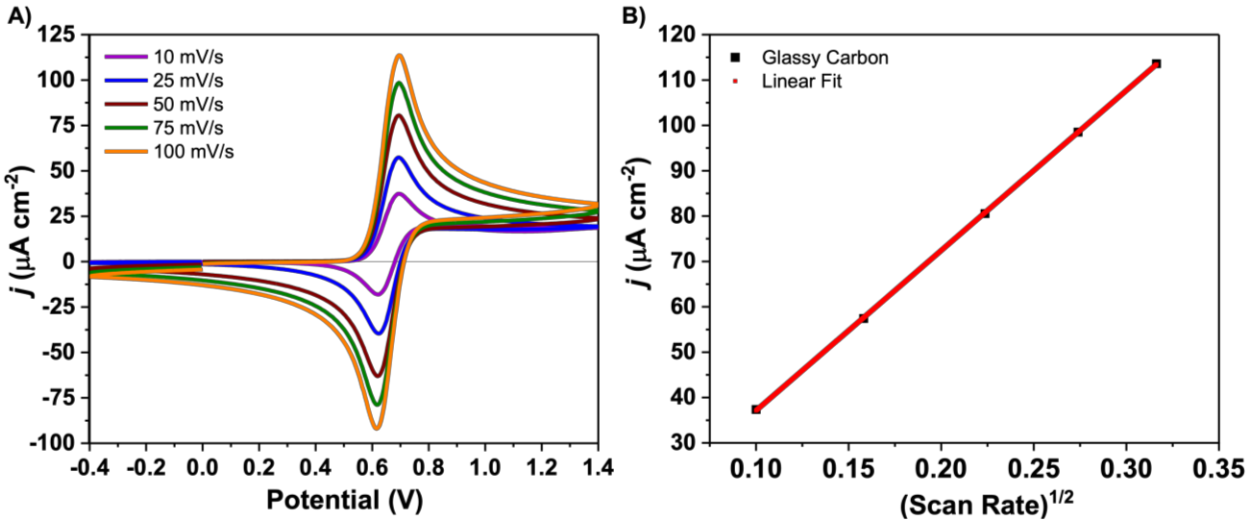

Figure 15. A) Cyclic voltammogram of a glassy carbon electrode measured at increasing scan rates in the presence of 5 mM TEMPO. B) Graph of photocurrent densities at the anodic peak vs. square root of scan rate with an associated line of best fit.

From this value, a steady state time of 300 seconds was calculated, which correlates to the time it takes TEMPO to diffuse from the generating electrode to the collecting electrode. Using this information, further CG experimentation was optimized to allow more than 300 seconds before the experiment was terminated. By tracking the movement of TEMPO in the solution, additional work on optimizing $BiVO_4$-based photoanodes can be conducted with a more complete understanding of how our redox mediator behaves.

Conclusion

This work demonstrates the inexpensive and facile fabrication of PEG-based $BiVO_4$ photoanodes to drive photoelectrosynthetic reactions. These photoanodes are quickly produced via a liquid-phase deposition method that utilizes the structure-directing agent, PEG, to produce semi-porous semiconductor crystals. The top-performing photoanode, FTO|$BiVO_4$(2.5%), obtained an average steady-state photocurrent density of 0.095 $\pm$ .04 mA cm^{-2} in an acetonitrile solution containing 5 mM TEMPO and 0.1 M $TBAPF_6$ under an applied bias of 0.3 V vs. SCE. While

exhibiting lower performance than previously described neat-$BiVO_4$ samples, these PEG-based photoanodes provide helpful information on the influence of structural morphology. Most notably, increasing PEG concentrations results in a decrease in film thickness and average particle size. As such, this work provides a framework as a proof of concept for future projects that optimize photoanode performance through structural manipulation.

Chapter II: Analysis of WO_3-$BiVO_4$ Heterojunction Solar Cells: Characterization and Incident Photon-to-Current Efficiency

Introduction

Following the characterization of PEG-based photoanodes, the focus shifted to improving the sluggish charge transfer properties of the $BiVO_4$ semiconductor surface. As described previously, $BiVO_4$ is known to undergo charge recombination that decreases its current generation during light-driven reactions.[1,23] To combat this loss of photocurrent, it was hypothesized that the addition of a second metal oxide, WO_3, in a layered heterojunction might facilitate more efficient charge transfer. WO_3 is of interest in this work due to its properties as an n-type semiconductor as well as its large band gap of 3.1 eV as compared to that of $BiVO_4$, with a band gap of 2.4 eV.[26-28] By pairing these two metal oxide layers, a band alignment is produced that promotes the flow of photo-excited electrons from the $BiVO_4$ layer into the WO_3 layer in an effort to reduce the effect of charge recombination.[17] It is important to note that there are three main types of semiconductor band alignments: Type I, II, and III (**Fig. 16**).

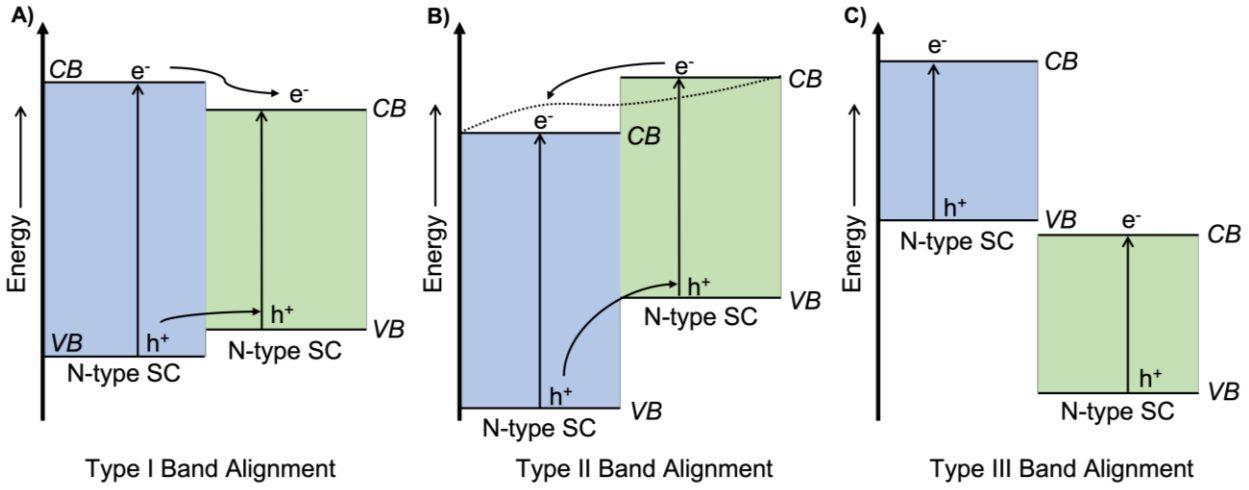

Figure 16. Energy band diagrams depicting the types of band alignments and associated electron movements possible when two n-type semiconductors are stacked. A) Type I, B) Type II, and C) Type III band alignments.

Type I band alignment, as shown in **Fig. 16a**, is the result of a high degree of overlap in band gap energies between two n-type semiconductors. Type I heterojunctions in our experimental setup would likely result in poor photocurrent generation due to the transport of charge away, rather than toward, the FTO electrode. A similar scenario occurs with type III band alignments (**Fig. 16c**) which are characterized by no overlap of band energies, leading to poor charge transfer to an FTO electrode. For these reasons, type I and III band alignments would likely result in decreased photocurrent generation. However, Type II heterojunctions (**Fig. 16b**) are promising solutions to facilitate the separation of charge by staggering two band gap energies that partially overlap.[29] This work describes a WO_3-$BiVO_4$ layered heterojunction, as shown in **Fig. 17**. By having the conduction band of $BiVO_4$ slightly more negative than WO_3, charge separation occurs, allowing for the transport of electrons toward the back contact.

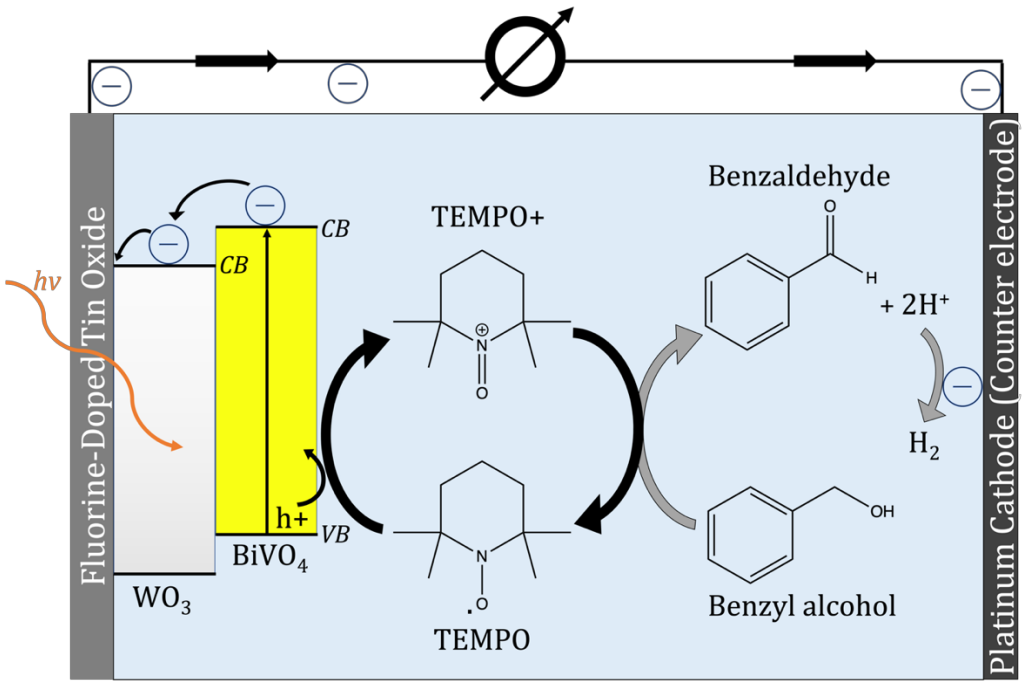

Figure 17. Schematic of WO_3-$BiVO_4$ photoanodes in solution illustrating the light-driven oxidation of TEMPO to $TEMPO^+$ in addition to the subsequent oxidation of benzyl alcohol to benzaldehyde. This diagram includes the FTO ohmic contact as well as the platinum cathode with labeled electron movement and cathodic hydrogen production.

Similarly, this band alignment facilitates the accumulation of holes at the $BiVO_4$ surface. As a result, WO_3-$BiVO_4$ heterojunctions exhibit several advantages over their individual components and could serve as an important step toward improving light-driven oxidation reactions.

This study characterizes the structure and photoelectrochemical properties of WO_3-$BiVO_4$ heterojunctions. UV-Vis and FESEM characterization were used to provide information about the properties of heterojunction materials and their possible benefits over individual components. Furthermore, the primary method of probing the photoelectrochemical performance of WO_3-$BiVO_4$ heterojunctions was via incident photon-to-current efficiency (IPCE) measurements. IPCE provides a measurement of how efficiently a photoanode can convert incident light into chemical energy at a given wavelength. By measuring this energy conversion efficiency for each of the individual components plus the WO_3-$BiVO_4$ heterojunction, a comparison can be made to better understand its usefulness as a light-active photoanode. Overall, this work describes the advantages of WO_3-$BiVO_4$ heterojunctions through comparisons of structural and photoelectrochemical properties of its individual component materials.

Methods

Materials

Bismuth (III) nitrate pentahydrate ($Bi(NO_3)_3 \cdot 5H_2O$, 99.999%), ammonium metavanadate (NH_4VO_3, ≥98.0%), tungsten (VI) chloride (WCl_6, ≥99.9%), benzyl alcohol (anhydrous, 99.8%), 2,2,6,6-tetramethylpiperidinyl-N-oxyl (TEMPO) (≥98%), acetonitrile (HPLC grade, VWR chemicals), nitric acid (70% pure in water, Acros Organics), and tetrabutylammonium hexafluorophosphate ($TBAPF_6$) (98%, Spectrum®) were used in this study. All chemicals outlined above were purchased from Sigma Aldrich unless otherwise noted. Ultrapure (18 MΩ) water was used for all aqueous solution preparations. Fluorine-doped tin oxide (FTO) glass (15 $\Omega\ cm^{-2}$) was

obtained from Hartford Glass Co. FTO, cut into 1 × 4 cm sections, and cleaned ultrasonically with ethanol for 15 minutes. Following this step, a second sonication was completed in 1:1 ethanol/acetone for 15 minutes. The FTO substrates were then dried with pure nitrogen gas before deposition.

Next, WO_3 samples were fabricated using a previously described procedure.[17] The WO_3 precursor solution contained 0.2 M of WCl_6 in 200-proof anhydrous ethanol. Anhydrous ethanol was prepared via drying with temperature-activated molecular sieves. Specifically, an Erlenmeyer flask containing 4Å molecular sieves was placed in an oven for 15 minutes at 180°C. Then, approximately 20 g of activated sieves were transferred to a Nalgene bottle, followed by the addition of 200 mL ethyl alcohol (200 proof, Pharmco). The solution was placed in a desiccator for at least 24 hours before use. To prepare the WO_3 solution, 12.7 mL of anhydrous ethanol was transferred via a micropipette to a 20 mL glass vial. Then, 0.9870 g of tungsten chloride (WCl_6) was added to the vial and left unsealed for five minutes under a fume hood. During this period, HCl gas readily evolves, and the reaction mixture will begin to turn dark blue. After the gas stops releasing from the solution, the vial was sealed and placed in a sonication bath for 10 minutes. Pre-cut FTO substrates were individually dipped and removed from the WO_3 precursor solution. Excess liquid was manually removed from the non-conductive side of the FTO and allowed to dry at room temperature until a blue film was obtained (~1 hour). Finally, the deposited samples were sintered at 450 °C for two hours, yielding a grey WO_3 film.

Following the fabrication of WO_3 samples, approximately half underwent a further fabrication procedure for the liquid-phase deposition of $BiVO_4$ to create a functional heterojunction.[30] To begin, a precursor solution of $BiVO_4$ was produced following a previously described procedure.[1] The $BiVO_4$ precursor consisted of 2 mmol $Bi(NO_3)_3$ and 2 mmol NH_4VO_3

(1:1 mole ratio) dissolved in 10 mL of 2 M nitric acid solution. NH_4VO_3 was first added to the nitric acid solution and sonicated for 10 minutes to fully dissolve the precursors. Then, $Bi(NO_3)_3$ was added, followed by an additional sonication for five minutes, yielding a yellow precursor solution. To fabricate $BiVO_4$ samples, a clean FTO substrate was dipped and removed from the precursor solution, allowing for an even, liquid-phase deposition. Similarly, WO_3-$BiVO_4$ heterojunctions were made by dipping a sintered FTO|WO_3 substrate into the yellow precursor solution to obtain a pre-sintered FTO|WO_3-$BiVO_4$ sample. All samples were allowed to air dry at room temperature until an orange film was obtained. Sintering at 450 °C for two hours yielded a bright yellow $BiVO_4$ film formed on the FTO|WO_3 substrate. Lastly, all FTO|WO_3-$BiVO_4$ (1L) samples were treated with a 1 M NaOH solution for 30 minutes, followed by a thorough rinse with ultrapure water and drying with a nitrogen stream. A second layer was deposited using the same protocol to produce the experimental heterojunctions, FTO|WO_3-$BiVO_4$ (2L).

Characterization Methods

UV-Vis measurements of all three sample types, FTO|WO_3, FTO|$BiVO_4$, and FTO|WO_3-$BiVO_4$ (2L), were collected with an Agilent Technologies Cary 60 spectrometer with baseline scans recorded with clean FTO only. Following the FTO control scans, experimental samples were tested sequentially following an identical sweep of visible light wavelengths from 900 nm to 200 nm. The band gap energy was then extrapolated from these observed absorption data using the Tauc method described previously. The morphology of the experimental samples was examined with a field emission scanning electron microscope (JEOL JSM6100) under an accelerated voltage of 5 kV.[17] Samples were sputtered with a 10 nm layer of gold prior to FESEM characterization.

Photoelectrochemical Methods

A WaveNow® potentiostat (Pine instruments) was used for photoelectrochemical measurements with a three-electrode configuration: a photoanode as a working electrode, an Ag/Ag^+ quasi-reference, and a Pt counter electrode at room temperature. As described previously, the Ag/Ag^+ quasi-reference was calibrated vs. ferrocenium/ferrocene after measurements and later converted to SCE with $E'_{Fc^+/Fc} = 0.45$ V vs. SCE. Illumination was conducted in a 10 mL volume with backside lighting of the working electrode (i.e., the light passed through the FTO before the WO_3-$BiVO_4$ heterojunction). The geometric surface area of all working electrodes in this study was measured at approximately 0.5 cm^2 to calculate the reported current density.

Incident photon to current efficiency (IPCE) was measured in acetonitrile with 0.1 M $TBAPF_6$ electrolyte, 5 mM TEMPO, 25 mM benzyl alcohol, and 100 mM pyridine. The current was measured under an applied bias of 0.6 V vs. SCE with 20 seconds on and 10 seconds off chopped illumination from a TLS-72-X300 monochromator (**Fig. 22**). Following this protocol, the wavelength was decreased during each 10-second off increment to ensure that each 20-second illuminated run used a different wavelength. Specifically, the wavelength was varied in the following manner: 700 nm → 540 nm via 20 nm intervals, 540 nm → 500 nm via 10 nm intervals, 500 nm → 400 nm via 5 nm intervals, and 400 nm → 350 nm via 10 nm intervals. The incident light power at each scanned wavelength was measured before the experiment using a Gentec-EO power meter equipped with a calibrated silicon photodiode detector. **Equation 4** was utilized to calculate IPCE at a given wavelength:

$$IPCE\ \% = \frac{1240 \times J}{P_\lambda \times \lambda} \times 100 \quad (4)$$

where J is the observed photocurrent density (A cm^{-2}), P_λ (W cm^{-2}) is the power of the monochromatic light at a measured wavelength, λ.

Results/Discussion

Fabrication of WO_3-$BiVO_4$ Electrodes

The following electrode types were fabricated using the previously described liquid-phase deposition technique: FTO|WO_3, FTO|$BiVO_4$ (2 layers, 2L), and FTO|WO_3-$BiVO_4$ (2L). FTO|WO_3-$BiVO_4$ (2L) heterojunctions were made by dipping a sintered FTO|WO_3 substrate into the yellow precursor solution to obtain a pre-sintered FTO|WO_3-$BiVO_4$ (1L) sample. Following sintering at 450°C for two hours, the electrodes were then treated with 1 M NaOH for 30 minutes to remove excess V_2O_5. Repeating these steps yielded an FTO|WO_3-$BiVO_4$ (2L) heterojunction electrode. A layer of epoxy was added to form circular working areas that were measured in order to calculate the photocurrent density of each sample type (**Figures 18a** and **18b**).

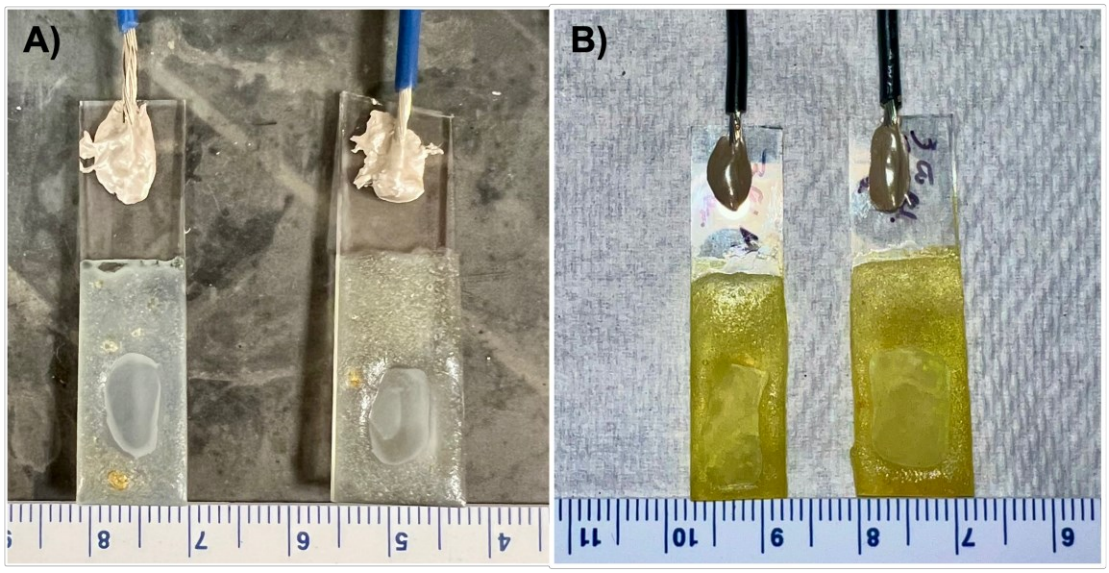

Figure 18. Images of electrode surfaces and experimental setup with labeled electrodes. A) Post-sintered FTO|WO_3 samples with epoxy applied to create circular working areas. B) Fabricated FTO|WO_3-$BiVO_4$ photoanodes with epoxy applied

Physical Characterization

Analysis of UV-Vis spectra (**Fig. 19**) indicated apparent visible light absorption for the three sample types: FTO|WO_3, FTO|$BiVO_4$ (2L), and FTO|WO_3-$BiVO_4$ (2L). However, the absorption of FTO|WO_3 (**Fig. 19b**) exhibited a blue-shift relative to other samples as its light absorption occurs at wavelengths < 440 nm, whereas typical $BiVO_4$ absorption occurs at ~490 nm (**Fig. 19a**).[1] The FTO|WO_3-$BiVO_4$ heterojunction (**Fig. 19c**) exhibited a light absorption onset of ~480 nm, slightly lower than that of FTO|$BiVO_4$ (2L). Band gaps determined for each sample type via Tauc plots matched reported values of 3.1 eV,[31] 2.4 eV,[1,6] and 2.5 eV,[32] for WO_3, $BiVO_4$, and WO_3-$BiVO_4$ respectively.

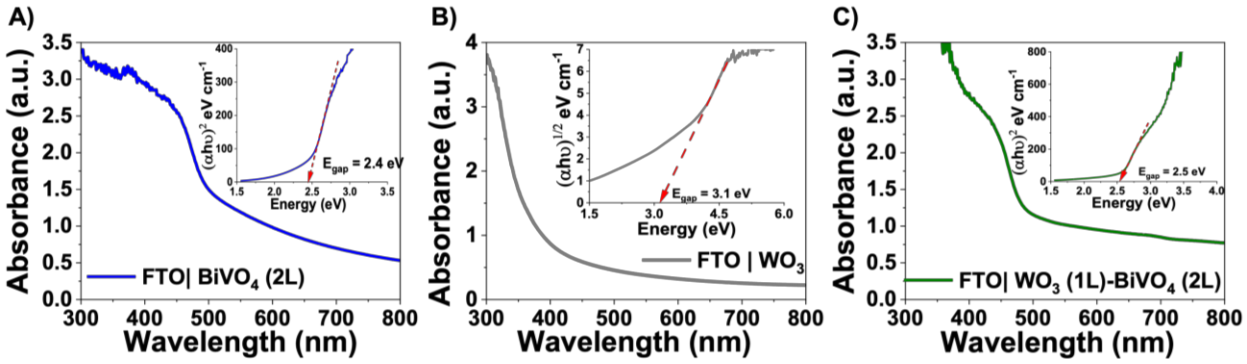

Figure 19. UV-visible absorption spectra of A) FTO|WO_3 (grey), B) FTO|$BiVO_4$ (2L) (blue), and C) FTO|WO_3-$BiVO_4$ (2L) (green) electrodes. The insets show corresponding Tauc plots with the indicated band gaps (E_{gap}).

Structural morphology was studied via field emission scanning electron microscopy. **Fig. 20a-b** shows top and cross-sectional views of single-layer FTO|WO_3 films. Further analysis yielded an average particle size of 68 $\pm$ 18 nm and a film thickness of 280 $\pm$ 15 nm. Deposition of tightly packed WO_3 films is critical in minimizing the amount of FTO exposure and ensuring a direct application of $BiVO_4$.[26,31-33] Furthermore, **Fig. 20c-d** shows top-down views of FTO|WO_3-$BiVO_4$ (2L), where $BiVO_4$ exhibits an aggregated network of particles with typical features of

monoclinic scheelite $BiVO_4$.[1] In previous work, a decrease in $BiVO_4$ aggregation when not deposited on WO_3 has been observed.[17] The cross-sectional views in **Fig. 20e-f** show a defined layering within the heterojunction and uniform covering of WO_3 and $BiVO_4$ on the FTO substrate. The overall thickness of the heterojunction was measured at 880 nm: 600 nm from the 2-layer $BiVO_4$ and 280 nm from the WO_3 single layer.

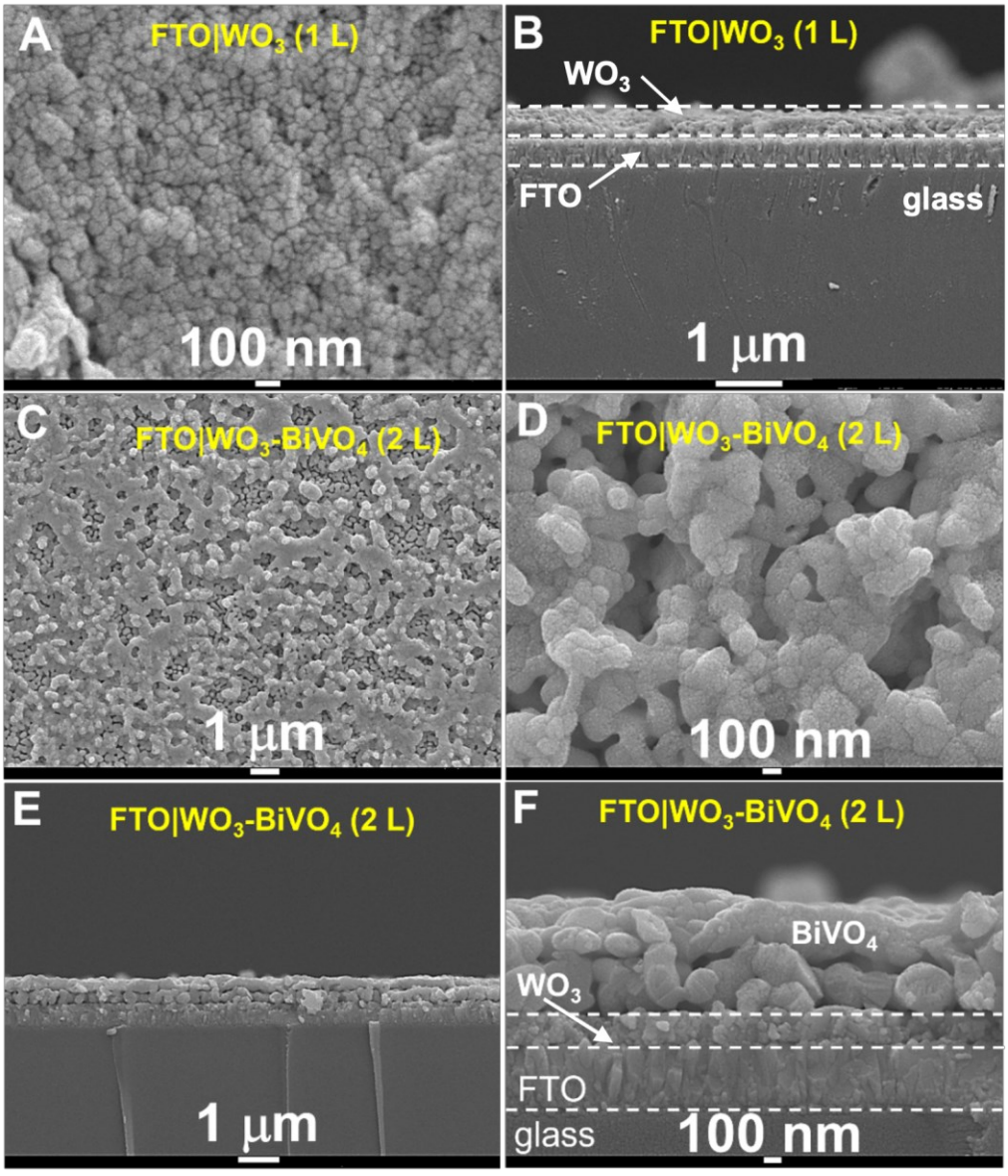

Figure 20. FESEM images of fabricated electrodes. A-B) Top and cross-section views of FTO|WO_3; C-D) Top-view images of FTO|WO_3-$BiVO_4$ (2L); E-F) Cross-section of FTO|WO_3-$BiVO_4$ (2L).

The deposition of two layers of $BiVO_4$ provides a maximal covering of the WO_3 to facilitate an effective spatial separation of the electron-hole pairs when the charge is transferred from one layer to the next.[34] Additionally, this covering ensures minimal contact of WO_3 with the electrolyte interface during light-driven reactions. Overall, SEM surface morphology showed a clear stacking of metal oxide semiconductors within the FTO|WO_3-$BiVO_4$ (2L) heterojunction electrodes.

Incident Photon to Current Efficiency Studies

Photoelectrochemical performance of the fabricated samples was measured using the incident photon-to-current efficiency (IPCE) technique. To calculate IPCE, transient photocurrent measurements were taken via chronoamperometry (CA) under an applied bias of 0.6 V vs. SCE at discrete wavelength intervals. The photoelectrochemical cell (**Fig. 21**) included a working electrode, an Ag/Ag^+ quasi-reference, and a Pt counter electrode in an acetonitrile solution with 0.1 M $TBAPF_6$, 5 mM TEMPO, 25 mM benzyl alcohol, and 100 mM pyridine.

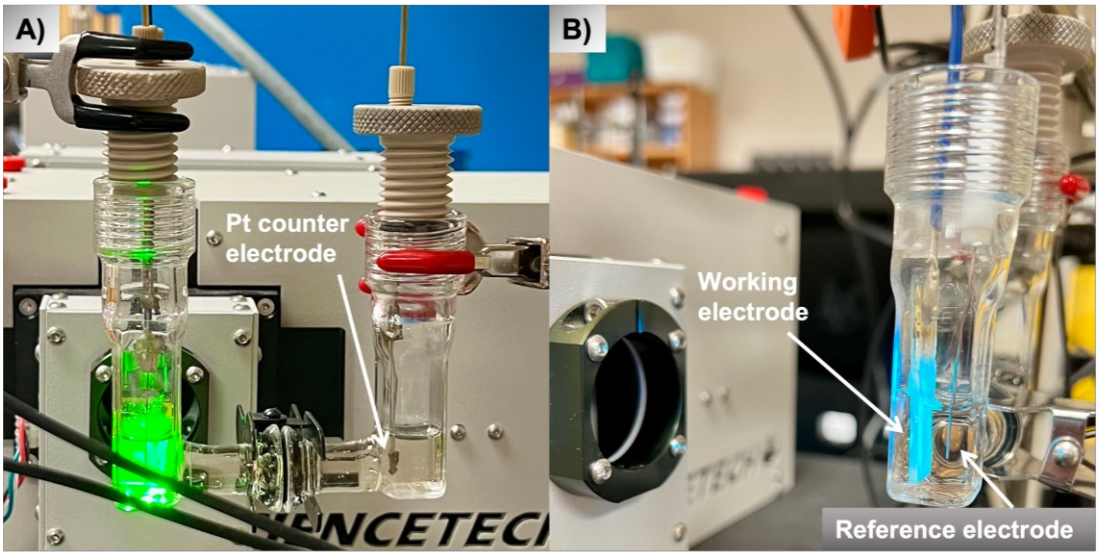

Figure 21. A) IPCE experimental setup with labeled Pt electrode. B) Side view of IPCE setup with labeled working and reference electrodes.

A photodiode was utilized to measure the incident power output of the monochromator, as shown in **Fig. 22d**. **Figures 22a-c** show transient photocurrent measurements from 440 nm → 480 nm, an active light-absorbing region for each sample type. The decreasing currents after illumination are evident in FTO|$BiVO_4$ (2L) (**Fig. 24b**) and are likely due to the accumulation of holes at $BiVO_4$ surface states and poor charge transfer kinetics.[1]

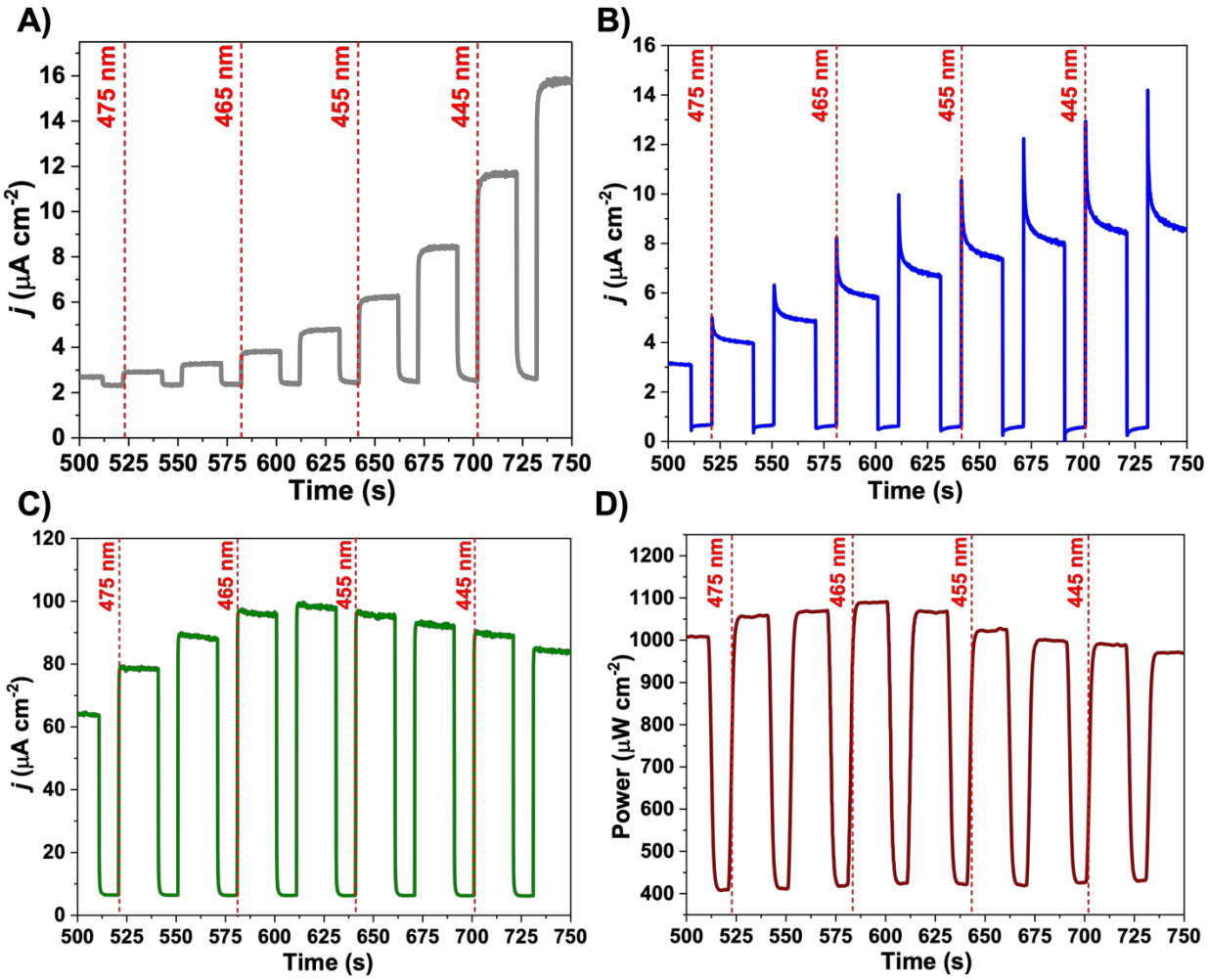

Figure 22. A-C) Transient photocurrent measurements of FTO|WO_3 (grey), FTO|$BiVO_4$ (2L) (blue), and FTO|WO_3-$BiVO_4$ (2L) (green) electrodes taken at a range of wavelengths with the light on and off. The electrodes were placed in an acetonitrile solution with 0.1 M $TBAPF_6$, 5 mM TEMPO, 25 mM benzyl alcohol, and 100 mM pyridine at 0.6 V vs. SCE applied potential. D) Incident light power was measured with a photodiode over a range of wavelengths with the light on and off.

Conversely, the plateauing onset current of FTO|WO_3 (**Fig. 22a**) and FTO|WO_3-$BiVO_4$ (2L) (**Fig. 22c**) corresponds to more efficient charge separation within the heterojunction, thus improving the sluggish charge transfer kinetics of $BiVO_4$ photoanodes.[23]

Following transient photocurrent measurements, the photodiode and CA result for each sample type were input into **Equation 4**. Photocurrent density was calculated relative to the working area of each experimental sample. By sweeping the wavelengths for both power output and observed photocurrent, the resultant IPCE % is expressed at each discrete wavelength tested. Individual metal oxides WO_3 and $BiVO_4$ have a photocurrent onset of ~450 nm and ~500 nm, respectively.[17] The heterojunction photoanode exhibited a slight red shift as photocurrent onset began at approximately 510 nm, as shown in **Fig. 23**.

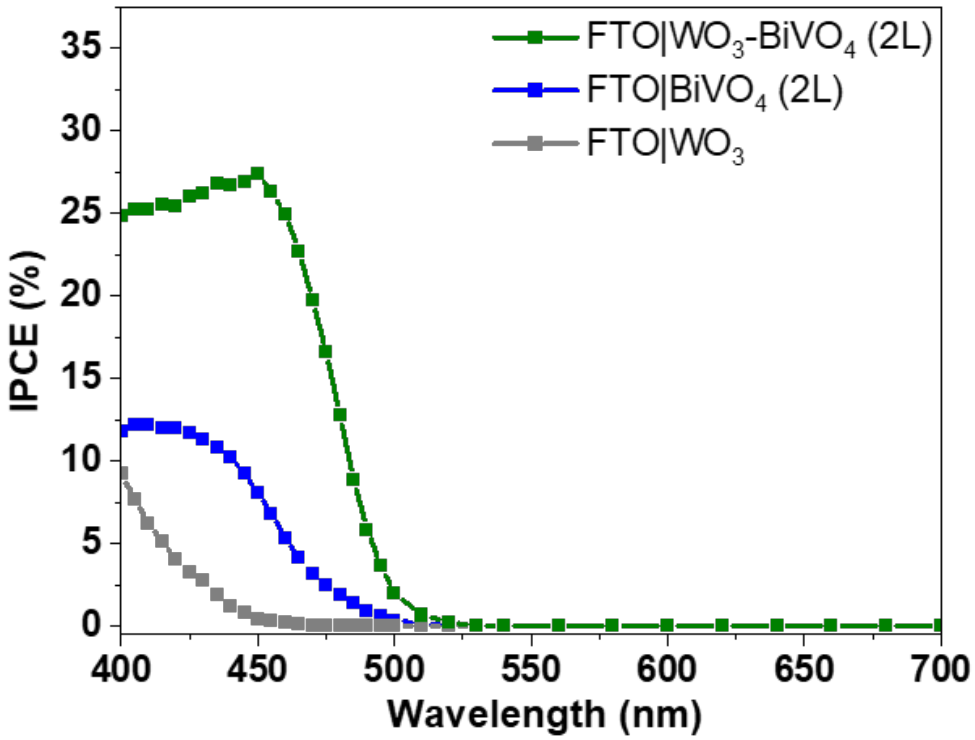

Figure 23. Incident photon-to-current efficiency (IPCE) percentage results for FTO|WO_3 (grey), FTO|$BiVO_4$ (2L) (blue), and FTO|WO_3-$BiVO_4$ (2L) (green) across 400 → 700 nm illumination.

Notably, IPCE % decreases at wavelengths shorter than 400 nm, likely the result of charge recombination of photo-promoted electrons in WO_3 with $BiVO_4$ holes.[27] As shown in **Table 2**, FTO|WO_3-$BiVO_4$ (2L) photoanodes exhibited the highest IPCE% of 28% at 420 nm wavelength light.

Table 2. Incident Photon-to-Current Efficiency of FTO|WO_3, FTO|$BiVO_4$ (2L), and FTO|WO_3-$BiVO_4$ (2L) Electrodes[a]

Sample Type	IPCE (λ = 450 nm)
FTO|WO_3	< 1%
FTO|$BiVO_4$ (2L)	5%
FTO|WO_3-$BiVO_4$ (2L)	28%

[a] Measurements performed in acetonitrile solution with 0.1 M $TBAPF_6$, 5 mM TEMPO, 25 mM benzyl alcohol, and 100 mM pyridine at 0.6 V vs. SCE applied potential.

Additionally, the IPCE % for FTO|$BiVO_4$ (2L) photoanodes closely resembles a previously reported value of ~12 %.[1] Overall, the fabricated heterojunction exhibited better performance than a linear combination of its components. This is likely due to the increased charge carrier dynamics typical of WO_3, along with efficient visible light absorption from $BiVO_4$.

Conclusion

This project describes a simple yet effective technique for fabricating WO_3-$BiVO_4$ heterojunctions for photoelectrosynthetic applications. Through a well-refined liquid phase deposition method, heterojunction photoanodes exhibiting consistent structure are easily reproducible. With the addition of WO_3 as an inner layer, a practical type II band alignment with $BiVO_4$ is produced, allowing for increased charge separation while minimizing destructive charge recombination. Furthermore, this project highlights the usefulness of calculating incident photon-

to-current efficiency for a better understanding of how well a photoanode converts incident photons into electrical energy. Fabricated heterojunctions consisting of WO_3-$BiVO_4$ exhibited an increased IPCE %, likely due to an increased charge separation facilitated by the WO_3 layer. Further work will focus on improving the IPCE % of developed photoanodes with the presence of an additional outer layer of nickel oxide (NiO) to enhance charge separation further while minimizing charge recombination.

References

1. Klinova McMillan, N.; Lopez, D. A.; Leem, G.; Sherman, B. D. $BiVO_4$ Photoanodes for TEMPO-Mediated Benzyl Alcohol Oxidation in Organic Media. *ChemPlusChem* **2022***, 87*, e202200187.

2. Timmaji, H. K. Bismuth-Based Oxide Semiconductors: Mild Synthesis and Practical Applications. *Environment Abstracts* **2011**; *73*, pp 112.

3. Zhang, Z.; Yates, J. T. Band Bending in Semiconductors: Chemical and Physical Consequences at Surfaces and Interfaces. *Chemical Reviews* **2012***, 112*, 5520-5551.

4. Xia, L.; Li, J.; Bai, J.; Li, L.; Zeng, Q.; Xu, Q.; Zhou, B. Preparation of a $BiVO_4$ Nanoporous Photoanode Based on Peroxovanadate Reduction and Conversion for Efficient Photoelectrochemical Performance. *Nanoscale* **2018***, 10*, 2848-2855.

5. Jia, Q.; Iwashina, K.; Kudo, A. Facile Fabrication of an Efficient $BiVO_4$ Thin Film Electrode for Water Splitting Under Visible Light Irradiation. *Proc. Natl. Acad. Sci.* **2012***, 109*, 11564-11569.

6. Park, Y.; McDonald, K. J.; Choi, K. Progress in Bismuth Vanadate Photoanodes for Use in Solar Water Oxidation. *Chemical Society Reviews* **2013***, 42*, 2321-2337.

7. Kim, T. W.; Choi, K. Nanoporous $BiVO_4$ Photoanodes with Dual-Layer Oxygen Evolution Catalysts for Solar Water Splitting. *Science* **2014***, 343*, 990-994.

8. Makuła, P.; Pacia, M.; Macyk, W. How To Correctly Determine the Band Gap Energy of Modified Semiconductor Photocatalysts Based on UV–Vis Spectra. *J. Phys. Chem.* **2018***, 9*, 6814-6817.

9. Huang, Z.; Pan, L.; Zou, J.; Zhang, X.; Wang, L. Nanostructured Bismuth Vanadate-Based Materials for Solar-Energy-Driven Water Oxidation: A Review on Recent Progress. *Nanoscale* **2014***, 6*, 14044-14063.

10. Ye, H.; Park, H. S.; Bard, A. J. Screening of Electrocatalysts for Photoelectrochemical Water Oxidation on W-Doped $BiVO_4$ Photocatalysts by Scanning Electrochemical Microscopy. *J. Phys. Chem. C* **2011***, 115*, 12464-12470.

11. Hernández, S.; Gerardi, G.; Bejtka, K.; Fina, A.; Russo, N. Evaluation of the Charge Transfer Kinetics of Spin-Coated $BiVO_4$ Thin Films for Sun-Driven Water Photoelectrolysis. *Applied Catalysis B: Environmental* **2016***, 190*, 66-74.

12. Chadderdon, D. J.; Wu, L.; Mcgraw, Z. A.; Panthani, M.; Li, W. Heterostructured Bismuth Vanadate/Cobalt Phosphate Photoelectrodes Promote TEMPO-Mediated Oxidation of 5-Hydroxymethylfurfural. *ChemElectroChem* **2019**, *6*, 3387-3392.

13. Reid, L. M.; Li, T.; Cao, Y.; Berlinguette, C. P. Organic Chemistry at Anodes and Photoanodes. *Sustainable Energy Fuels* **2018***, 2*, 1905-1927.

14. Semmelhack, M. F.; Chou, C. S.; Cortes, D. A. Nitroxyl-Mediated Electrooxidation of Alcohols to Aldehydes and Ketones. *J. Am. Chem. Soc.* **1983***, 105*, 4492-4494.

15. Herath, A. C.; Becker, J. Y. 2,2,6,6-Tetramethyl piperidine-1-oxyl (TEMPO)-Mediated Catalytic Oxidation of Benzyl Alcohol in Acetonitrile and Ionic Liquid 1-butyl-3-methyl-imidazolium hexafluorophosphate [BMIm][PF6]: Kinetic Analysis. *Electrochim. Acta* **2008***, 53*, 4324-4330.

16. Tran-Phu, T.; Chen, H.; Bo, R.; Di Bernardo, I.; Fusco, Z.; Simonov, A. N.; Tricoli, A. High-Temperature One-Step Synthesis of Efficient Nanostructured Bismuth Vanadate Photoanodes for Water Oxidation. *Energy technology (Weinheim, Germany)* **2019***, 7*, 1801052.

17. McMillan, Nelli Klinova, Wortley, Jacob, Nguyen, Khanh, Lopez, Diego A., Leem, Gyu, Sherman, Benjamin D. Heterojunction WO_3-$BiVO_4$ Photoanodes for TEMPO-Mediated Benzyl Alcohol Oxidation and Hydrogen Production in Organic Media. **2023***, manuscript in preparation*.

18. Liu, W.; Srivastava, V.; Kurley, J. M.; Jiang, C.; Talapin, D. V. Thermal Stability of Semiconductor Nanocrystal Solids: Understanding Nanocrystal Sintering and Grain Growth. *J. Phys. Chem. C* **2022***, 126*, 21136-21148.

19. Fardush Tanha, J.; Farhad, S. F. U.; Honey, U.; Tanvir, N. I.; Hasan, T.; Shahriyar Nishat, S.; Kabir, A.; Ahmed, S.; Hakim, M.; Khan, M. N. I.; Moniruzzaman, M.; Ahmed, I. A DFT+U Look into Experimentally Synthesized Monoclinic Scheelite $BiVO_4$. *J. Appl. Phys.* **2021***, 130*, 235107.

20. Andrade, T. S.; Sá, B. A. C.; Oliveira, A. T.; Bruziquesi, C. G. O.; Salomão, P. E. A.; Rodriguez, M.; Nogueira, F. G. E.; Alves de Oliveira, L. C.; Pereira, M. C. W:$BiVO_4$-WO_3-V_2O_5 Heterostructures Increase Light Absorption and Charge Transport in Photoanodes for Water Splitting. *Journal of Environmental Chemical Engineering* **2022***, 10*, 107278.

21. Cooper, J. K.; Gul, S.; Toma, F. M.; Chen, L.; Liu, Y.; Guo, J.; Ager, J. W.; Yano, J.; Sharp, I. D. Indirect Bandgap and Optical Properties of Monoclinic Bismuth Vanadate. *J. Phys. Chem. C* **2015***, 119*, 2969-2974.

22. Barhdadi, R.; Comminges, C.; Doherty, A. P.; Nédélec, J. Y.; O'Toole, S.; Troupel, M. The Electrochemistry of TEMPO-Mediated Oxidation of Alcohols in Ionic Liquid. *J. Appl. Electrochem.* **2007***, 37*, 723-728.

23. Peter, L. M.; Wijayantha, K. G. U.; Tahir, A. A. Kinetics of Light-Driven Oxygen Evolution at α-Fe_2O_3 Electrodes. *Faraday Discuss.* **2012***, 155*, 309-322.

24. Rettie, A. J. E.; Lee, H. C.; Marshall, L. G.; Lin, J.; Capan, C.; Lindemuth, J.; McCloy, J. S.; Zhou, J.; Bard, A. J.; Mullins, C. B. Combined Charge Carrier Transport and Photoelectrochemical Characterization of BiVO4 Single Crystals: Intrinsic Behavior of a Complex Metal Oxide. *J. Am. Chem. Soc.* **2013***, 135*, 11389-11396.

25. Sherman, B. D.; Sheridan, M. V.; Dares, C. J.; Meyer, T. J. Two Electrode Collector–Generator Method for the Detection of Electrochemically or Photoelectrochemically Produced O_2. *Anal. Chem.* **2016***, 88*, 7076-7082.

26. Grigioni, I.; Dozzi, M. V.; Selli, E. Photoinduced Electron Transfer in $WO_3/BiVO_4$ Heterojunction Photoanodes: Effects of the WO3 Layer Thickness. *J. Phys. Condens Matter* **2020***, 32*, 014001-648X/ab440b. Epub 2019 Sep 12.

27. Grigioni, I.; Stamplecoskie, K. G.; Jara, D. H.; Dozzi, M. V.; Oriana, A.; Cerullo, G.; Kamat, P. V.; Selli, E. Wavelength-Dependent Ultrafast Charge Carrier Separation in the WO3/BiVO4 Coupled System. *ACS Energy Lett.* **2017***, 2*, 1362-1367.

28. Grigioni, I.; Stamplecoskie, K. G.; Selli, E.; Kamat, P. V. Dynamics of Photogenerated Charge Carriers in WO3/BiVO4 Heterojunction Photoanodes. *J. Phys. Chem. C* **2015***, 119*, 20792-20800.

29. Zheng, Z.; Zu, X.; Zhang, Y.; Zhou, W. Rational Design of Type-II Nano-Heterojunctions for Nanoscale Optoelectronics. *Materials Today Physics* **2020***, 15*, 100262.

30. Cheng, W.; Baudrin, E.; Dunn, B.; Zink, J. I. Synthesis and Electrochromic Properties of Mesoporous Tungsten Oxide. *J. Mater. Chem.* **2001***, 11*, 92-97.

31. Khoomortezaei, S.; Abdizadeh, H.; Golobostanfard, M. R. Triple Layer Heterojunction WO3/BiVO4/BiFeO3 Porous Photoanode for Efficient Photoelectrochemical Water Splitting. *ACS Appl. Energy Mater.* **2019***, 2*, 6428-6439.

32. Coelho, D.; Gaudêncio, J. P. R. S.; Carminati, S. A.; Ribeiro, F. W. P.; Nogueira, A. F.; Mascaro, L. H. Bi Electrodeposition on WO3 Photoanode to Improve the Photoactivity of the $WO_3/BiVO_4$ Heterostructure to Water Splitting. *Chem. Eng. J.* **2020***, 399*, 125836.

33. Zheng, G.; Wang, J.; Liu, H.; Murugadoss, V.; Zu, G.; Che, H.; Lai, C.; Li, H.; Ding, T.; Gao, Q.; Guo, Z. Tungsten Oxide Nanostructures and Nanocomposites for Photoelectrochemical Water Splitting. *Nanoscale* **2019***, 11*, 18968-18994.

34. Moniz, S. J. A.; Shevlin, S. A.; Martin, D. J.; Guo, Z.; Tang, J. Visible-Light Driven Heterojunction Photocatalysts for Water Splitting – a Critical Review. *Energy Environ. Sci.* **2015***, 8*, 731-759.